

Structural characterization of potentially seismogenic faults in the Fort Worth Basin

Elizabeth A. Horne¹, Peter H. Hennings¹, Johnathon L. Osmond², and Heather R. DeShon³

Abstract

From 2006 through mid-2018, there have been 125 $M_w \geq 2.5$ recorded earthquakes within the Fort Worth Basin and the Dallas-Fort Worth metropolitan area. There is general scientific consensus that this increase in seismicity has been induced by increases in pore-fluid pressure from wastewater injection and from cross-fault pore-pressure imbalance due to injection and production. Previous fault stress analyses indicate that many of the faults are critically stressed; therefore, careful consideration should be taken when injecting in close proximity to these structures. Understanding the structural characteristics that control geomechanical aspects of these earthquake-prone faults is vital in characterizing this known hazard. To improve understanding of faults in the system, we have developed a characterization using a new basin-wide fault interpretation and database that has been assembled through the integration of published data, 2D and 3D seismic surveys, outcrop mapping, earthquakes, and interpretations provided by operators resulting in a 3D structural framework of basement-rooting faults. Our results show that a primary fault system trends northeast–southwest, creating a system of elongate horsts and grabens. Fault architectures range from isolated faults to linked and cross-cutting relay systems with individual segments ranging in length from 0.5 to 80 km. The faults that have hosted earthquakes are generally less than 10 km long, trend toward the northeast, and exhibit more than 50 m of normal displacement. The intensity of faulting decreases to the west away from the Ouachita structural front. Statistical analysis of the fault length, spacing, throw, and linkage tendency enables a more complete characterization of faults in the basin, which can be used to mitigate the seismic hazard. Finally, we find that a significant percentage of the total population of faults may be susceptible to reactivation and seismicity as those that have slipped recently.

Introduction

The Fort Worth Basin (FWB) is a prolific petroleum province, where hydrocarbons have been produced from several stratigraphic intervals conventionally and unconventionally since the early 1900s (Ball and Perry, 1996; Pollastro et al., 2007). Since 2000, the Mississippian-age Barnett Shale Formation in the FWB has been one of the most productive shale-gas resource plays within Texas (Jarvie et al., 2007; Pollastro et al., 2007; Ikonnikova et al., 2014). Like other shale-gas resource plays, large volumes of wastewater have been produced in addition to hydrocarbons. In the core Barnett-producing area, the wastewater has been injected into strata underlying the Barnett using saltwater disposal wells (SWDs). The widespread use of SWDs has been linked to elevated seismic activity in the FWB and in other unconventional basins in the south-central United States (McGarr et al.,

2002; Ellsworth, 2013). This has particularly been an issue in northeastern Oklahoma where vast volumes of wastewater have been disposed into equivalent strata, which has been suggested to be the cause of the increase in seismicity experienced in that region since 2009 (e.g., Shah and Keller, 2017; Kolawole et al., 2019). Specifically, from 2006 through mid-2018, there have been 125 $M_w \geq 2.5$ with the largest event recorded as M_w 4.0 within the FWB, impacting the Dallas-Fort Worth (DFW) metropolitan area (USGS, TexNet, SMU EQ catalogs). The spatial and temporal relationships between earthquake sequences, SWDs, major roads, and urban population centers, as well as the location of the FWB within the state of Texas in the USA, are shown in Figure 1.

Earthquake history

Earthquakes in the FWB have occurred primarily in discrete spatial clusters (Quinones et al., 2019), mostly

¹The University of Texas at Austin, Bureau of Economic Geology, 10611 Exploration Way, Austin, Texas 78758, USA. E-mail: lily.horne@beg.utexas.edu (corresponding author); peter.hennings@beg.utexas.edu.

²The University of Texas at Austin, Bureau of Economic Geology, 10611 Exploration Way, Austin, Texas 78758, USA and University of Oslo, Department of Geosciences, P.O. Box 1047, Blindern, 0316 Oslo, Norway. E-mail: johnathon.osmond@utexas.edu.

³Southern Methodist University, Department of Earth Sciences, Dallas, Texas, USA. E-mail: hdeshon@mail.smu.edu.

Manuscript received by the Editor 6 September 2019; revised manuscript received 10 December 2019; published ahead of production 27 January 2020; published online 11 March 2020. This paper appears in *Interpretation*, Vol. 8, No. 2 (May 2020); p. T323–T347, 21 FIGS., 7 TABLES.

<http://dx.doi.org/10.1190/INT-2019-0188.1>. © 2020 Society of Exploration Geophysicists and American Association of Petroleum Geologists. All rights reserved.

adjacent to previously mapped faults. Five named earthquake sequences have been studied using local seismic network data: the 2008–2009 DFW Airport (Frohlich et al., 2010, 2011; Frohlich, 2012; Janská and Eisner, 2012; Reiter et al., 2012; Ogwari et al., 2018), the 2009 Cleburne (Justinic et al., 2013), the 2013–2014 Azle-Reno (Hornbach et al., 2015), the 2015–2017 Irving-Dallas (Frohlich et al., 2010, 2011; Ogwari et al., 2018), and the 2015 Mw 4.0 Venus (Scales et al., 2017) (Table 1). Most earthquakes produce normal faulting focal mechanisms associated with northeast-striking faults (Magnani et al., 2017). Detailed studies indicate that many of the sequences began prior to the first felt events and/or generated

small-magnitude earthquakes well past the original felt earthquakes (Reiter et al., 2012; Magnani et al., 2017). Local and regional seismic networks have routinely reported data for the basin since December 2013 to supplement the USGS catalog (DeShon et al., 2018; Savvaidis et al., 2019). Many of the earthquake sequences listed generated seismicity through 2018, and several new clusters have developed (DeShon et al., 2018).

The vast majority of FWB earthquake hypocenters are located beneath the Precambrian basement-sediment interface (Frohlich et al., 2011; Hornbach et al., 2015; Magnani et al., 2017; Scales et al., 2017; Quinones et al., 2018, 2019; Hennings et al., 2019). Of the approximately 10 named sequences, only the Azle-Reno earthquake events have been located above the basement-sediment interface (Hornbach et al., 2015). There is general scientific consensus that this increase in seismicity has been induced by elevated pore-fluid pressure from SWDs into sedimentary injection intervals that are in hydrogeologic continuity with local and regional basement-rooting faults and from cross-fault pore-pressure imbalances due to injection and production (e.g., Ellsworth, 2013; Zhang et al., 2013; Gono et al., 2015; Weingarten et al., 2015; Hornbach et al., 2016; Chen et al., 2018; Hennings et al., 2019).

Geologic setting

The FWB is an elongate, asymmetric flexural foreland basin that formed as one of several basins in the foreland of the advancing Ouachita orogenic belt during the Late Mississippian through Pennsylvanian epochs (Flawn, 1959; Ewing, 1991; Pollastro et al., 2007; Bruner and Smosna, 2011; George, 2016; Leary et al., 2017; Magnani et al., 2017; Poole et al., 2017). The basin is bounded to the east and southeast by the northwest-verging Ouachita orogenic fold and thrust belt, and to the north by an array of high-angle reverse faults that follow the southwestern margins of the Muenster and Red River arches (Figure 2). These northern bounding structural arches grew prior to and in sequence with the development of the FWB in the foreland of the Ouachita orogenic belt, which migrated progressively northward over the basin (Flawn, 1959; Ewing, 1991; Pollastro et al., 2007; Bruner and Smosna, 2011; George, 2016; Leary et al., 2017; Magnani et al., 2017; Poole et al., 2017). The FWB is deepest in the northeast, with more than 3675 m (12,000 ft) of preserved sediment infill adjacent to the

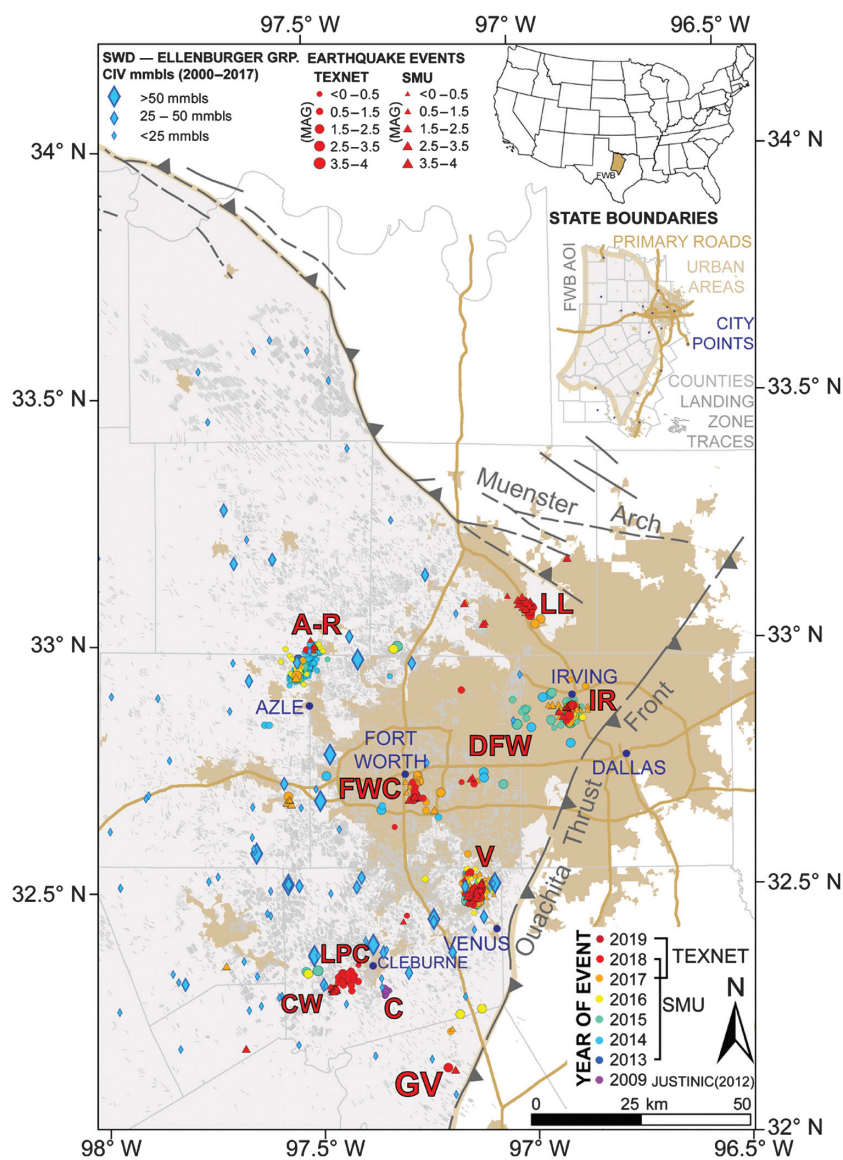


Figure 1. Map of earthquake hypocenters located within the greater FWB by TexNet and SMU researchers, which are shown as triangles and circles, respectively. Hypocenter colors reflect the year of the event. The earthquake sequences are labeled as A-R, Azle-Reno; FWC, Fort Worth City; CW, Cleburne West; LPC, Lake Pat Cleburne; C, Cleburne; V, Venus; DFWA, Dallas-Fort Worth Airport; IR, Irving; LL, Lake Lewisville. Both hypocenter data sets have graduated sizes, reflecting the increasing event magnitude.

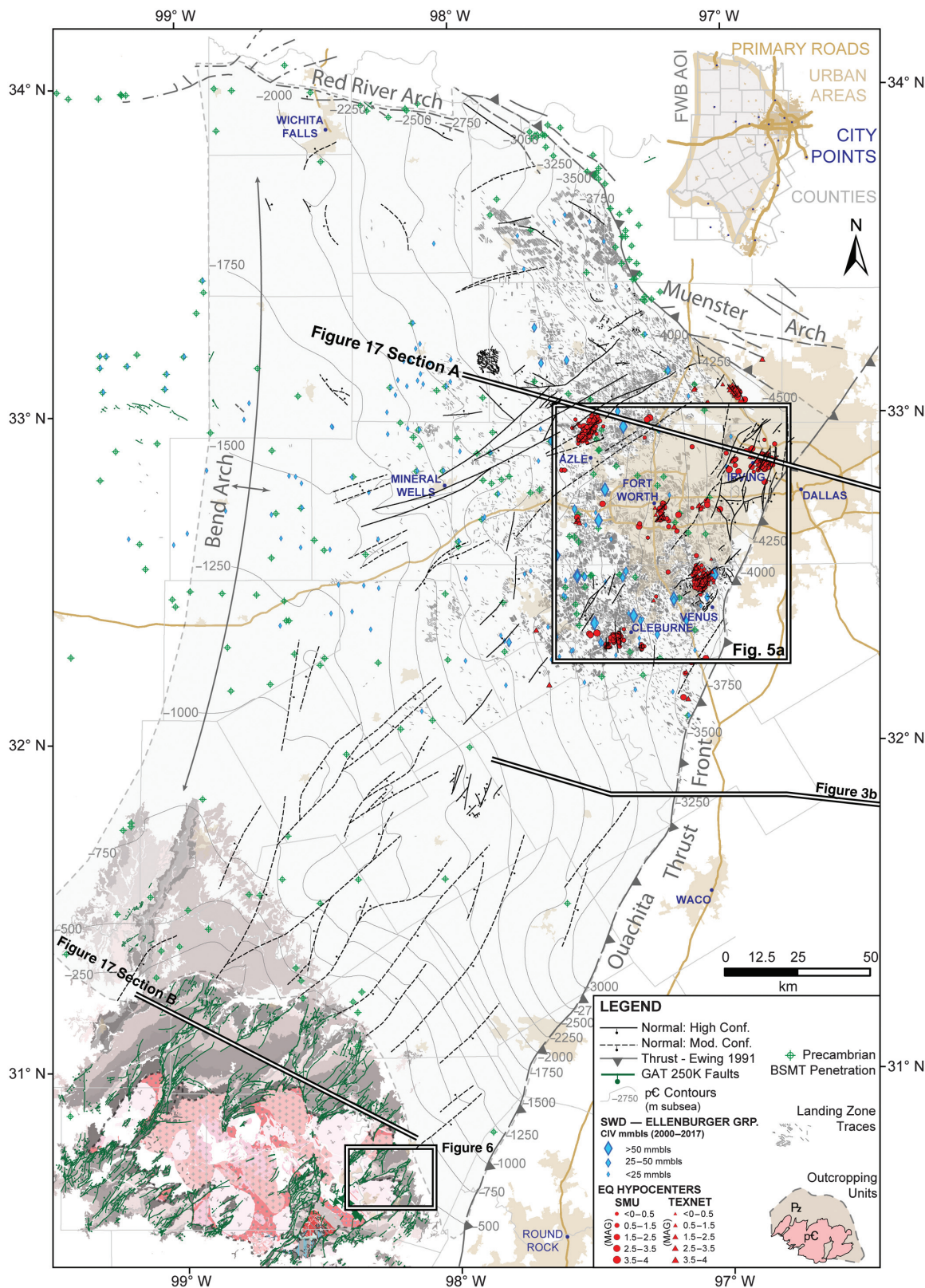


Figure 2. Map showing the greater FWB and LU study area. Earthquake hypocenters located by TexNet and SMU researchers are shown as red triangles and circles, respectively. Both hypocenter data sets have graduated sizes, dependent on the earthquake magnitude. The resultant interpretations of basement-rooting normal fault traces are shown as the solid and dashed black traces, symbolizing high- and moderate-confidence interpretations, respectively. The approximate traces for the Muenster Arch and Ouachita thrust front, fault zones are highlighted as the gray-dashed polylines, and the teeth symbols signify the upthrown hanging-wall block for the respective fault zones. The outcropping fault traces are shown in dark green.

Muenster Arch and Ouachita thrust front and is shallowest in the south, where the lateral equivalent of the basin's deepest stratigraphic intervals outcrop along the Precambrian basement-cored Llano Uplift (LU) (Figure 3a and 3b).

In general, deformation within the FWB is expressed as northeast-trending, high-angle normal faults that have generally linear map traces and run subparallel to the Ouachita thrust front (Figure 2). A majority of these

faults also root into the Precambrian crystalline basement, and the mechanism for deformation has been attributed to basin-wide flexure generated by the loading of the overriding Ouachita orogenic belt (Figure 3b) (Walper, 1982; Viele and Thomas, 1989; Alsalem et al., 2017). Field observations, active-source seismic imaging, and well correlations show that this deformation extends from the Precambrian-age crystalline basement into the sedimentary succession but does not breach the uncon-

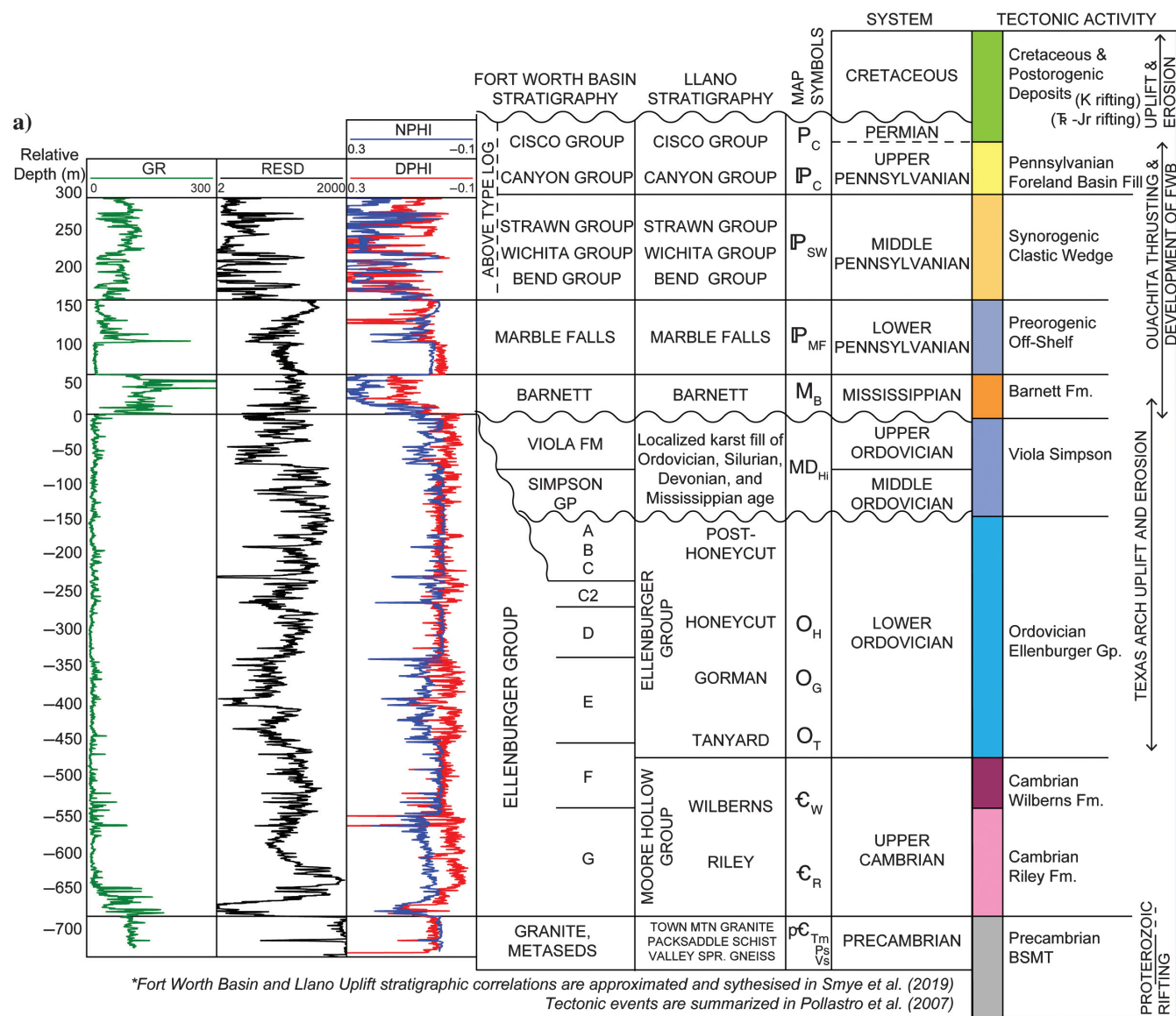


Figure 3. (a) Type log and schematic regional tectonostratigraphic events for the FWB and LU study area, modified after Smye et al. (2019). (b) Schematic east-west cross section of the tectonic boundary between the Ouachita fold-and-thrust belt and the FWB region, modified after Ewing (1991) after Nicholas and Waddell (1989).

formity that separates Pennsylvanian and Cretaceous rocks. This suggests that these faults have not experienced significant dip-slip movement since their formation in the Late Paleozoic (Magnani et al., 2017).

Prior to the development of the FWB, this region was located on the margin of the Laurentian continent that experienced Late Proterozoic and Cambrian rifting (Walper, 1982; Thomas, 2004; Whitmeyer and Karlstrom, 2007; Hennings et al., 2019; Smye et al., 2019). These events are reflected in pre-Ouachita orogenic sedimentary facies and as Precambrian basement lithologies (e.g., Barnes and Bell, 1977; Barnes and Rose, 1981; Wilkerson et al., 1988; Walker, 1992; Carlson and Reese, 1994; Roback, 1996; Carlson, 1998; Reese et al., 2000; Reese and Mosher, 2004). This Late Proterozoic- and Cambrian-age rift margin trends to the northeast and is roughly parallel to the trend of the FWB axis and the Ouachita thrust front. This northeasterly trend is also manifested as the dominant strike for basement-rooting faults within the FWB (Figure 2). Many of these faults may be attributed to Proterozoic extension, and they may be subsequently reactivated due to tectonic loading of the Ouachita thrust front. Reactivation along these pre-existing planes may have facilitated the propagation of younger, shallower fault extensions into previously unfaulted Paleozoic strata. Additionally, there are faults within the sedimentary succession that have concentric strike orientations and are generally smaller (mostly <2 km strike length), which originated from collapse of karst features within the carbonate-rich Ordovician Ellenburger Group (Hardage et al., 1996b; Loucks, 2003; Sullivan et al., 2006; McDonnell et al., 2007; Qi et al., 2014). These karst systems are pervasive throughout the region (e.g., Aktepe et al., 2008; Elebiju et al., 2010; Khatiwada et al., 2013), but the relationship among basement faults, karstification, and karst-related faulting is not addressed here.

Previous work

Some, but not all, of the major earthquake sequences are near SWDs and several comprehensive geologic and hydrogeologic simulation models have been generated for causal analysis. These analyses include basin-wide stratigraphic and petrophysical correlations to determine porosity and permeability fairways for target injection intervals (Smye et al., 2019), as well as hydrogeologic simulation studies to estimate the magnitude of pore-pressure change that is possible within the FWB from SWD (Gono et al., 2015; Hornbach et al., 2016; Quinones et al., 2019). Previous work on fault distribution conducted in the FWB used a similar multidisciplinary database to build an integrated fault framework (Hennings et al., 2019). The nature of seismicity within this basin has been postulated to be wastewater injection-induced, rather than naturally occurring (Magnani et al.,

2017). This determination has been further supported through studies that aimed to understand the balance of many controlling variables (e.g., the rate of injection, production, spatial and temporal distribution of seismicity relates to the subsurface faulted architecture, etc.) that enable triggered earthquake events.

Specifically, research by Hennings et al. (2019) provides an updated analysis of the regional stress state and modernized the understanding of the structural architecture of the basin. Their work identifies and verifies 251 basement-rooting fault segments that were integrated with a new stress model to probabilistically determine their fault slip potential (FSP) (e.g., Walsh et al., 2017). The stress state in the northern FWB is normal — strike-slip/normal faulting ($A_{\phi} = 1.2$) and transitions to normal faulting in the south ($A_{\phi} = 0.8$) (Lund Snee and Zoback, 2016; Quinones et al., 2018; Hennings et al., 2019). The general trend of S_{Hmax} , has a northeast azimuth, sub-parallel to the dominant direction of fault strike, providing favorable conditions for a majority of faults in the basin to be highly stressed and sensitive to stress change. To investigate the changes in Pp associated with fault reactivation and earthquakes at a regional scale, a comprehensive geologic model and hydrogeologic simulation of SWD injection intervals and the Barnett Shale-producing intervals are required and are also out of the scope of this study. The fault interpretations presented herein are an update of the prior work outlined above as this research included additional field and subsurface data which was leveraged to provide a comprehensive structural characterization and analysis.

Basement-rooted normal faults in the FWB under the population centers of the DFW metropolitan area, reactivated by petroleum industry activities, pose a clearly identified seismic hazard. Herein, we synthesize all available geologic information on these faults, characterize their structural traits, and provide a database that can be used for further study and to mitigate the hazard of seismicity.

Fault interpretation and modeling Data and methods

A 3D framework of the faulted Precambrian basement was generated through the integration of field

Table 1. Earthquake hypocentral events for discrete sequences grouped by year.

EQ sequence — fault	Abbreviation	2008	2009	2013	2014	2015	2016	2017	2018	2019
Azle — Reno	AR					Mw 3.6				
Cleburne — Justinic 2012	C									
Cleburne — West	CW									
Dallas Fort Worth Airport	DFWA					Mw 3.6				
Fort Worth City	FWC									
Grandview	GV									
Irving	IR					Mw 3.5				
Lake Lewisville	LL									
Lake Pat Cleburne	LPC									
Venus	V					Mw 4.0				

Note: Significant earthquake events occurred in 2015 for several sequences, and the magnitudes for these events have been annotated.

and subsurface data sets and following interpretation methods outlined by [Krantz and Neely \(2016\)](#). The areal extent of the faulted framework model is approximately 62,000 km², and the variable quality, resolution, and spatial extent of available control data have resulted in a patchy network of faults whose character (orientation, length) and intensity (deformation offset, frequency) reflect the uneven distribution of control data throughout the basin. The interpretation is derived primarily from the public domain because a majority of the subsurface data and interpretation products for the FWB remain proprietary. Data sources include interpretations from seismic reflection data conducted in-house and provided externally by petroleum operators, point locations of earthquake hypocenters and orientations calculated from focal mechanism solutions, and the digital integration of all publicly available data, including maps, cross sections, existing fault interpretations, and interpretations from thousands of digital and raster well logs that were sourced from the RRC website ([Railroad Commission of Texas, 2016](#)) and IHS LogNet.

As with all integrated data sets, it is important to recognize the spatial limitations of each data source. In this model, the resolution and strength of information obtained from each data source have been considered and sources of data with increasing spatial completeness, reliability, resolution, and quality are delineated using areal interpretation domains: ID1–5 as shown in Figure 4. The data sources, interpretation methods, and resulting fault confidences are listed in Table 2, which have been modified as compared to [Hennings et al. \(2019\)](#).

Specifically, segments have been qualitatively classified according to levels of confidence: high, moderate, and low. High-confidence fault segments have enough data to validate their mapped geometry. Moderate-confidence fault segment interpretations have varying degrees of uncertainty about their present state that should be considered. These uncertainties may include their current mapped extent (length, height), geometry, lateral continuity, or specific placement. Finally, faults that are classified as low confidence lack sufficient evidence

based on our interpretation to warrant inclusion into the final fault map and 3D model. In many cases, faults that were originally mapped in previous studies have been included in our final map. The map view fault traces may be unmodified, but our analysis has provided additional constraints that alter the interpretations in 3D. Detailed descriptions for each interpretation domain ID are provided in the following subsections. Additionally, fault segments are grouped into several families, delineated by regional extent, resolution, and shared data sources (Table 2).

Subsurface interpretation domains

ID1

The first and largest interpretation domain, ID1, is shown in light gray in Figure 4. This region covers

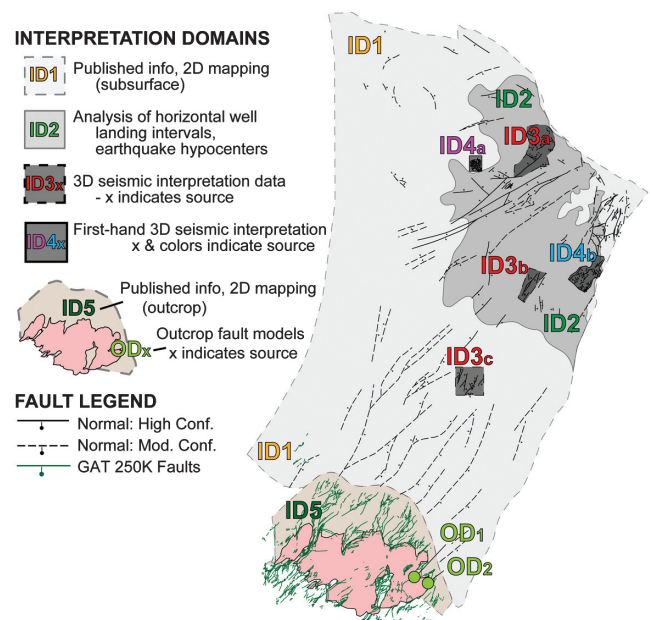


Figure 4. Index map of interpretation domains (ID1–5 and OD1–2). ID1–4 regions rely on subsurface data sets. Data locations ID5, OD1, and OD2 use outcrop exposures.

Table 2. Data set and methodology used in the fault interpretation.

Fault interpretation data and methodology		IDs	Confidence	Fault family colors and names
1	Outcrop interpretation by the authors	OD	Faults with High confidence N:142	3D from outcrop (LLANO UPLIFT)
2	Published outcrop interpretation	ID5		2D from PUB (LLANO UPLIFT)
3	Earthquakes from dense monitoring arrays and detailed velocity models	ID2		3D from PUB, LZ and EQ
4	Data from 3D seismic interpretation verified by the authors	ID4		3D from SEISMIC (VENUS)
5	Published 3D seismic data interpretation using trusted methods	ID3		3D from SEISMIC (OTHER)
6	Interpretation of 3D seismic data completed by the authors	ID4		3D from SEISMIC (BOONSVILLE)
7	First-hand 3D mapping of 21,000+ horizontal wells	ID2	Faults with moderate confidence N:201	3D from PUB, LZ and EQ
8	Published 2D seismic data interpretation verified by the authors	ID2		3D from PUB, LZ and EQ
9	Published 2D seismic data interpretation using trusted methods	ID2		3D from PUB, LZ and EQ
10	Fault maps submitted to the TX-RRC developed using trusted methods	ID2		3D from PUB, LZ AND EQ
11	Mapping of 1286 vertical wells correlated by the authors	ID1		2D from PUB (FORT WORTH BASIN)
12	Published mapping of vertical wells verified by the authors	ID1		2D from PUB (FORT WORTH BASIN)

Note: Fault family names and colors referenced in later figures are also indicated. Modified after [Hennings et al. \(2019\)](#).

72% (approximately 45,500 km²) of the FWB. Faults within this interpretation domain were identified previously (Belforte, 1971; Thompson, 1982; Ewing, 1991; Hentz et al., 2012; Eastman and Murin, 2016) and subsequently modified here. These fault segments have been verified by horizon mapping using stratigraphic correlations from 1286 control wells (Smye et al., 2019) as well as projecting observations and interpretations from outcrop exposures from the northeastern margin of the LU (Kier et al., 1976; Barnes and Rose, 1981; Kier, 1988; Ewing, 1991). Fault panes were generated from 2D polylines by applying an average dip angle normal to the trend of each line. The up- and down-thrown sides of the fault segments are clearly observable in these data; however, a majority of the segments proposed in this areal domain lack data with sufficient dip constraints. For this reason, the 41 fault traces proposed within ID1 are considered as being of moderate confidence.

ID2

Faults grouped into interpretation domain ID2 are supported by a more robust data set than ID1. This region is shown as a medium-gray shade and covers approximately 25% (approximately 16,000 km²) of the FWB (Figure 4). There are nearly 21,000 horizontal wells within this data region, which represents the core of the Barnett Shale-producing area (Figure 1). Abrupt linear changes in elevation are prevalent among the horizontal legs of wells targeting the Barnett Shale, which imply the presence of displaced Paleozoic layers and support the interpretation of previously unmapped faults (Hennings et al., 2019). The methodology used to generate the interpretation of the landing zones (LZ) for each horizontal well was described by Dommissie (2013) and Dommissie et al. (2018). In addition to using LZ trends, new faults were interpreted within ID2 by integrating earthquake hy-

pocentral data from the SMU Earthquake Catalog (Hornbach et al., 2015; Magnani et al., 2017; Scales et al., 2017; Ogwari et al., 2018) and the TexNet Earthquake Catalog (Savvaidis et al., 2019). An example of how accurately located earthquake events were used to define fault segment surfaces is shown for the Irving and Azle seismogenic sequences (Figure 5b and 5c, respectively).

In addition to earthquake-defined faults, previously mapped fault segments were verified from published studies (Elebiju et al., 2010; Howe, 2012; Justinic et al.,

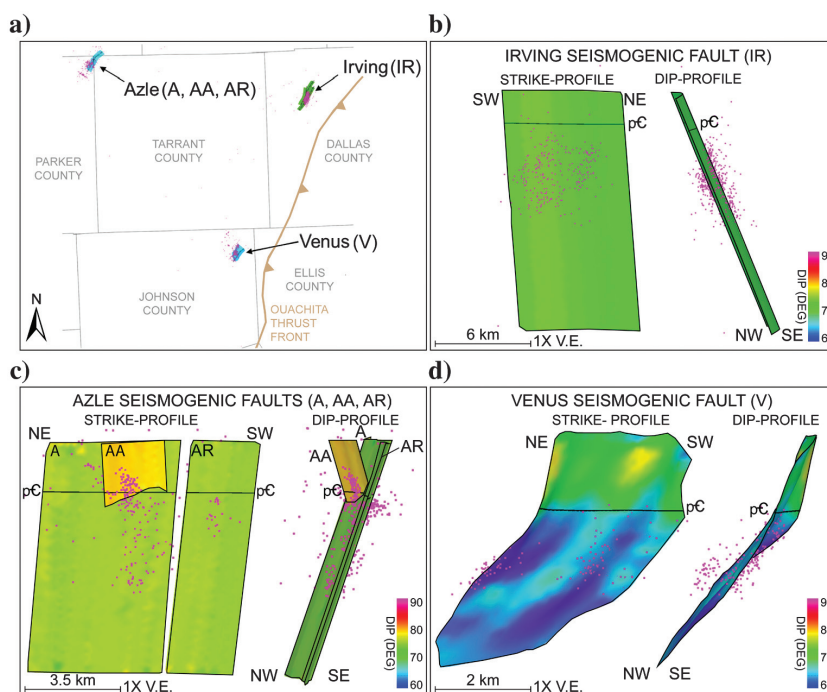


Figure 5. Selected seismogenic faults in the FWB modeled in three dimensions. (a) Inset map of the northern FWB showing key examples of known seismogenic faults as surfaces interpreted in three dimensions; the inset map is outlined in Figure 2, (b) highlights one of the Irving seismogenic faults (IR), (c) shows three fault segment surfaces associated with the Azle earthquake sequence (A, AA, and AR), and (d) shows the main seismogenic fault of the Venus earthquake sequence (V). The Azle and Irving fault surfaces are associated with ID2, but the Venus fault segment is part of ID4b. The black line that bisects each fault surface represents the basement-sediment interface. Pink dots represent earthquake hypocentral events that were used to define the plane of each seismogenic fault. The 3D seismic data were used to interpret the shallow portions of the Venus fault in (d).

Table 3. Average orientations, length, throw, and confidence by fault family.

Fault family colors and names	#	Strike (°)	Dip (°)	Length (m)			Throw (m)			Confidence		
				Average	Max	Min	Average	Max	Min	# high	# mod	
FWB	2D from PUB	41	037°	71.5°	28,660	87,219	2940	130.2	285	45.4	0	41
	3D from PUB, LZ, and EQ	85	015.3°	72.6°	13,387	73,552	1783	99	454	13.2	54	31
	3D from SEISMIC (OTHER)	53	034°	72.2°	3,342	16,853	693	59.5	193.6	15.5	53	0
	3D from SEISMIC (VENUS)	35	046.6°	73.2°	2,652	9,546	551.3	51.86	206.7	8	35	0
	3D from SEISMIC (BOONSVILLE)	129	130.7°	70.7°	855	2,023	261.5	21.1	88	4	0	129
	EQ faults	18	024.5°	72.6°	9,390	51,488	2120	70.7	275.3	31	8	10
LU	2D from PUB	1654	048.7°	72.2°	2,472	33,970	51	NA	NA	NA	1654	0
	HOOVER POINT	261	043°	72.32°	NA	NA	NA	0.41	7.94	0.001	261	0
	LHOIST QUARRY	116	036°	71.9°	NA	NA	NA	NA	NA	NA	116	0

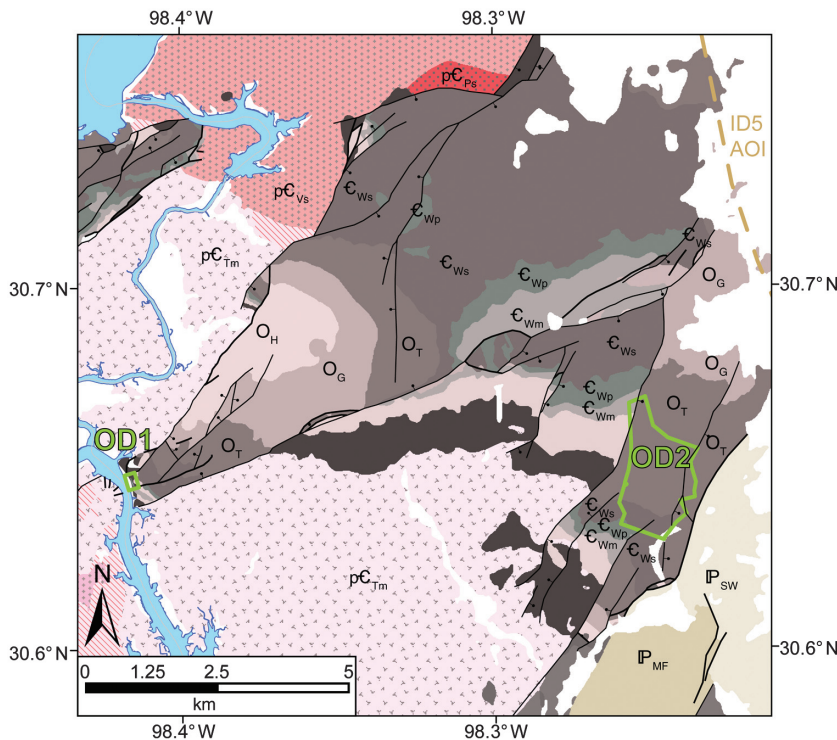


Figure 6. Inset map of the northeastern LU. See Figure 2 for the location and symbols. The fault traces and stratigraphic unit polygons are modified after the Geologic Atlas of Texas (USGS TWSC). The 3D outcrop models of Hoover Point (OD1) and Lhoist Quarry (OD2) are outlined in green. Precambrian basement lithologies are shown in variations of pink and are juxtaposed by Paleozoic strata, shown in gray.

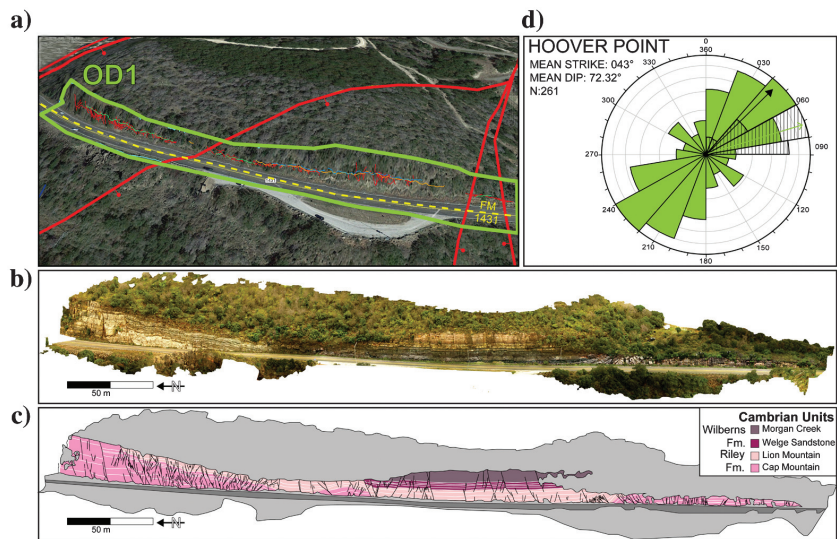


Figure 7. Panoramic image and interpretation of the Hoover Point outcrop (OD1): (a) The approximate extent of the 3D outcrop model is highlighted in a Google Earth image, looking obliquely toward the northeast, (b) high-resolution aerial drone image of the Hoover Point road cut, (c) interpreted aerial drone image with fault trace interpretations shown as black lines ($N > 261$), stratigraphic units are shown as solid colors, continuous bedsets are outlined in various colored polygons, and vegetation has been grayed out, and (d) rose diagram of primary faults mapped from Hoover Point ($N = 261$) with green petals representing ranges in the strike orientation, black arrow showing the mean strike, black-striped petals showing ranges in the dip, and green arrow showing the mean dip.

2013). Map and cross-section interpretations included in the Railroad Commission hearing Docket 09-0296411 (2016) provided constraints on 3D fault geometries. Similar to faults within ID1, dip angles for a majority of the proposed segments are difficult to determine due to insufficient data. Nevertheless, ID2 consists of 85 fault segments, 22 of which have been newly interpreted using offset horizontal legs in the LZ analysis, whereas 14 new fault segments have been interpreted entirely from earthquake hypocenters. Specifically, earthquake hypocenters define the planes of three faults in the Azle earthquake sequence, four faults near the town of Cleburne, four faults in Irving and Dallas, two faults near Lake Lewisville, and one fault within the Venus sequence (Figure 1). The remaining 49 fault segments are either verified from high-confidence published sources or have been adapted from previous publications using observations from LZ analyses and earthquake hypocenters. Overall, the discrepancy in data quality for fault segments within ID2 has resulted in the classification of 54 high-confidence fault segment interpretations, and 31 moderate-confidence interpretations.

ID3

There are three separate regions labeled ID3 in Figure 4 (ID3a-c). These regions are spatially limited and cumulatively only cover 1.5% (approximately 900 km²) of the total area of the subsurface mapped region. Though small, these data regions contain fault interpretations from 2D and 3D depth-migrated and depth-converted proprietary reflection seismic data provided by operators and from publications that have the finest scale of control from the published domain (Elebiju et al., 2010; Patterson, 2010; Khatiwada et al., 2013). When combined, 53 fault segments are validated within these data regions, all of which are classified as high-confidence 3D interpretations.

ID4

Faults within interpretation domains ID4a and ID4b were interpreted by the authors using depth-converted 3D reflection seismic data (ID4a) and on interpretations provided by operators (ID4b). Similar to ID3, the areal coverage of

ID4 regions are <1% (approximately 512 km²) of the footprint of the total FWB framework model. Interpretations from the ID4a and ID4b subregions have the greatest completeness and have the finest scale of control.

The data set used to analyze region ID4a is comprised of a depth-migrated 3D seismic reflection volume, whose data cover approximately 65 km². This data set covers a portion of the conventional Boonsville gas field and is located in a region where tectonic faults and karst-related faulting has been reported to coexist. This juxtaposition of karst-related faulting and tectonic faults is assumed to be consistent throughout the subsurface as well as in outcrop (Hardage et al., 1996a; Sullivan et al., 2006; Jarvie et al., 2007; Pollastro et al., 2007; Hentz et al., 2012). The components of this subsurface data set are outlined in Hardage (1996), and observed deformation patterns have been described in the literature (Hardage et al., 1996a, 1996b; Sullivan et al., 2006; McDonnell et al., 2007; Alhakeem, 2013). An interpretation of basement-rooting faults was conducted using this data set. The degree of karstification is extensive, and it degrades the seismic reflection image quality along the underlying basement-sediment interface, resulting in the interpretation of up to 129 basement-rooted faults with moderate confidence. Whereas these faults may not all be basement-rooted, they still constitute risk for reactivation and seismicity.

The second domain, ID4b, is located in northeastern NE Johnson County near the town of Venus, Texas. Similar to ID4a, this region provides a more complete assessment of faults due to first-hand interpretation by the authors (see also Hennings et al., 2019). This interpretation domain includes a high-quality, proprietary 500 km² depth-migrated 3D seismic volume, which resulted in the interpretation of 35 basement-rooting fault segments that are classified as high confidence. Figure 5d illustrates how the Venus seismogenic fault surface was constrained by the 3D seismic data above the basement-sediment interface and how it then follows earthquake hypocenters to deeper levels.

Summary of subsurface interpretation domains

With all interpretation domains considered, 343 fault segments are identified in the subsurface of the FWB. Due to the spatial unevenness, resolution, and reliability of data, 142 fault segments are classified as high-confidence fault interpretations. The remaining 201 segments

are classified as having a moderate level of confidence because there is evidence for the existence of these segments but important characteristics of the faults (i.e., the 3D orientation, length, displacement) cannot be sufficiently constrained with the current database. Fault trends are well constrained for fault traces of high and moderate confidence; however, many mapped segments lack sufficient dip constraints. These data gaps necessitated the integration of field observations and measurements of proximal outcropping fault zones exposed along the north and northeastern margin of the LU.

Outcrop interpretation domains

The southern margin of the FWB coincides with the north and northeastern margin of the LU (Figure 2). The LU is a dome-shaped structural high, which exposes the Precambrian basement, the lower Paleozoic

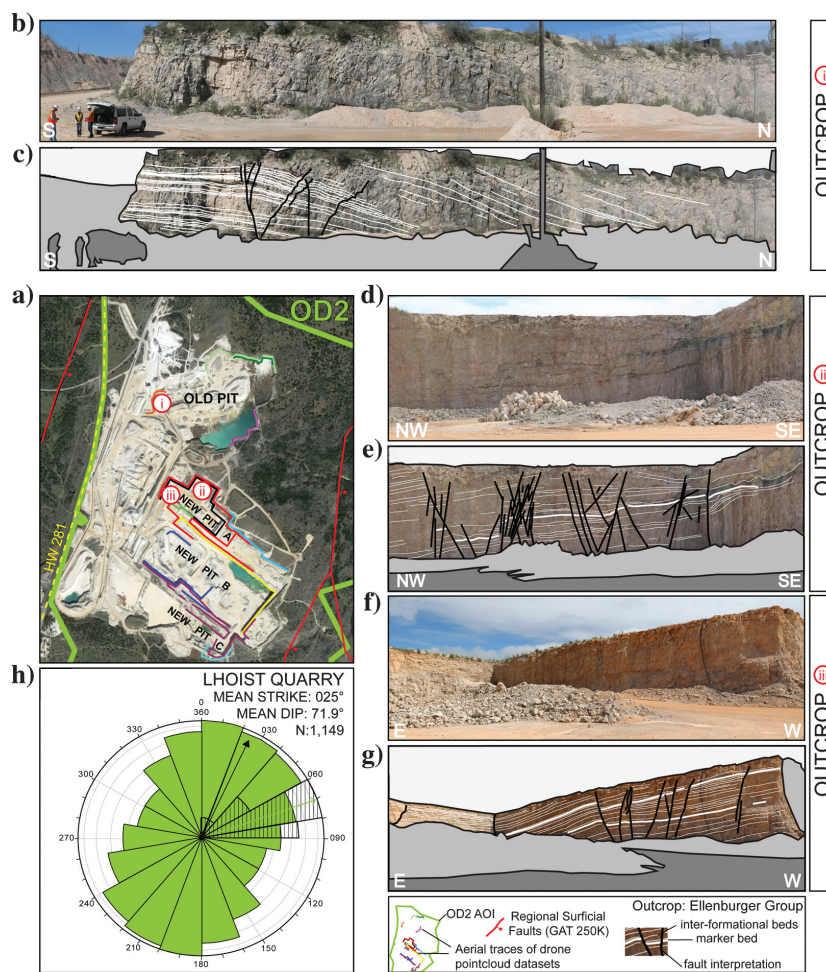


Figure 8. Three outcrop exposures have been selected to highlight changes in deformation within the quarry (b-g). (a) Inset map of the Lhoist Quarry, (b, d, and f) show high-resolution images, and (c, e, and g) represent outcrop interpretations. Fault traces are shown as black lines, and bedding planes are shown as white lines. The bold white lines signify key marker beds, and vegetation has been grayed out. (h) A rose diagram of faults mapped from all fault surfaces mapped in Lhoist Quarry is shown, with green- and black-striped petals representing ranges in strike and dip angles, respectively. The black arrow points to average strike, and the green arrow shows the mean dip.

sedimentary section, and the northeast-trending faults of Pennsylvanian age that are genetically part of the adjacent FWB. The stratigraphic and structural elements exposed in the LU are summarized in great detail throughout the published literature (e.g., Paige, 1912; Cloud and Barnes, 1946; Flawn, 1959; Freeman and Wilde, 1964; Bell and Barnes, 1972; Nicholas and Rozendal, 1975; Barnes, 1982; Barnes and Bell, 1977; Barnes and Rose, 1981; Kier, 1988; Hatcher et al., 1989; Amsbury and Haenggi, 1991, 1993; Ewing, 1991). Fault seg-

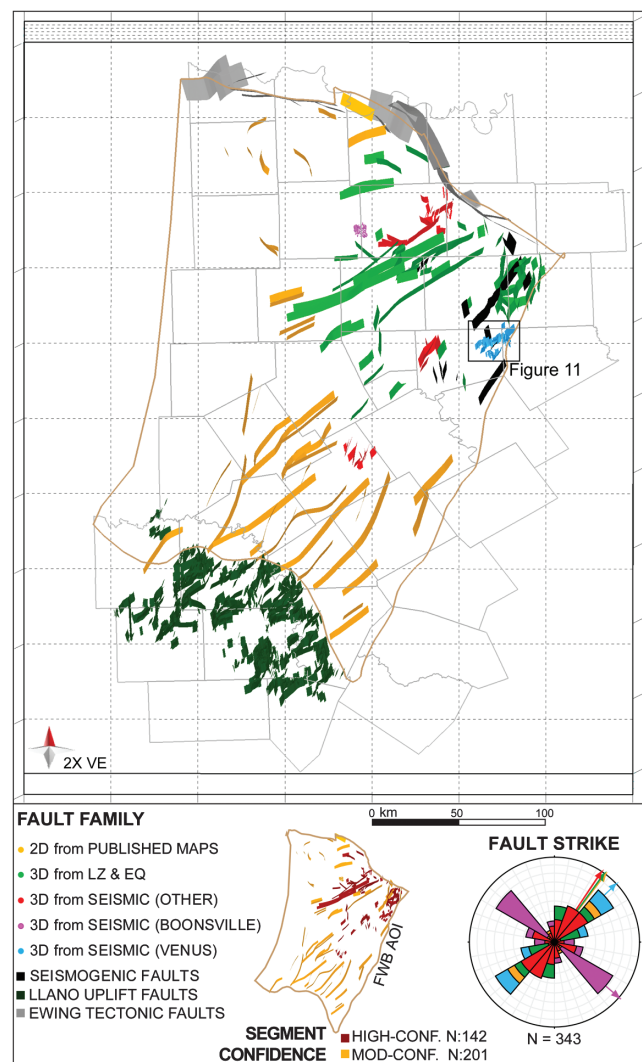


Figure 9. Oblique view of the 3D faulted framework of the greater FWB. Fault surfaces are colored depending on their associated fault family: blue, 3D seismic (Venus); magenta, 3D seismic (Boonsville); red, 3D seismic (other); green, 3D published, LZ, and earthquake faults; yellow, 2D published; and gray, Llano Outcrop published. Known seismogenic faults are shown as black surfaces. The fault surfaces vary in height, dependent on the data source. Faults interpreted in ID1–3 have a fault height of approximately 4 km, extending from 1.5 above and clipped 2.5 km below the basement-sediment interface. Fault segments within ID4 have heights that are determined by interpretations conducted by the authors. The rose diagram plots the range in strike for each fault family, colored according to the respective group.

ment traces, bedding contacts, and their respective field measurements along the northeastern margin of the LU have been gleaned from these previous studies and integrated into the digital database. The areal extent of this data region is represented by ID5 (Figure 4).

ID5

Interpretation domain ID5 is located along the north and northeastern margin of the LU. ID5 spans the entirety of this LU outcrop domain and contains 1654 individual fault segment traces compiled by the Geologic Atlas of Texas (USGS TWSC). These faults have been compiled from previously published fault interpretations (e.g., Kier et al., 1976; Barnes and Rose, 1981; Ewing, 1991), the results of which have been characterized according to fault geometry orientation (strike, dip) and length. However, the vast majority of mapped faults in the LU region are generally concentrated along exposures of sedimentary rocks. It is presumed that the decrease in the number of identified faults in areas where only metamorphic and igneous rocks are present is a result of mapping bias because identifying faults in the field without stratigraphic piercing points or discernible field relationships can be difficult in vegetated or developed areas. Therefore, the number of map-scale faults may be larger, and the fault trace length and orientation data may be incomplete to some extent. Nevertheless, these attributes are compared to subsurface fault data sets and provide a spatial link and a geometric proxy between subsurface and outcrop fault models (Table 3). In two key areas, 3D orthorectified models were generated using photographs taken by aerial drones to gain a better understanding of the 3D character of the fault systems at the outcrop scale (Figures 2 and 6). The first is a roadside-outcrop referred to as Hoover Point (OD1), and the second location is known as the Lhoist Quarry (OD2) (Figure 6).

Although all segments within ID5 maintain a high-confidence classification, they are not included in the generation of the 3D faulted crystalline basement surface and fault framework model because it is out of the scope of this research.

OD1 — Hoover Point

The Hoover Point outcrop is a road cut located along road FM 1431 (Amsbury et al., 1994; Johnson, 2004). This exposure is approximately 460 m in length, and trends NW-SE (Figure 6). The outcrop is situated between two large normal faults that dip toward each other, forming a graben that is intersected by a third prominent fault (Figure 7a). A high-resolution panoramic image is used to interpret stratigraphic and deformation elements of the Hoover Point outcrop (Figure 7b). The stratigraphic units exposed are the Cambrian Cap Mountain Limestone and Lion Mountain Sandstone members of the Riley Formation and Welge Sandstone and Morgan Creek Members of the Wilberns Formation (Figures 3 and 7c).

There are 261 high-angle, throughgoing normal faults interpreted along the outcrop, whose strike orientations

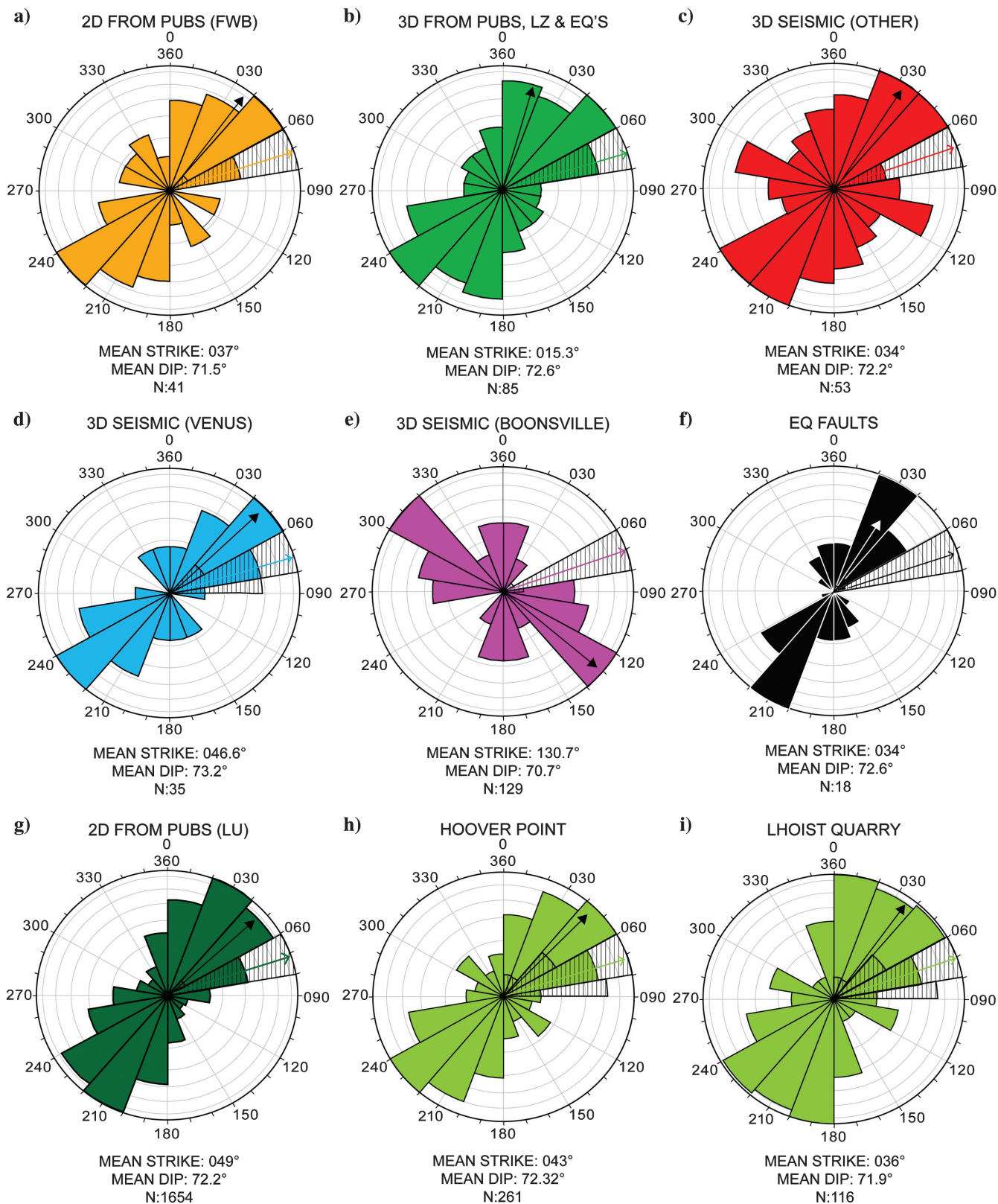


Figure 10. Rose diagrams of fault strike for analyzed fault families. The colored petals represent ranges in the strike, and the black-striped petals show ranges in the dip magnitude. The colored arrows show the average dip, and the black arrows point in the direction of the mean strike. The dip magnitudes are plotted within the 0°–90° quadrant of each rose diagram.

gradually rotate from northeast to east, orthogonal to the outcrop face. The mean strike of faults at this outcrop is 043° , but there is a small number of faults with other orientations (Figure 7d). The faults dip between 60° and 80° , and the mean dip is 72.3° . Although the vertical and lateral lengths of the faults cannot be determined from these data, given the existence of a predominant set of faults with a similar strike to regional faults, it can be postulated with some confidence that the faults comprise an interconnected network in three dimensions.

OD2 — Lhoist Quarry

The Lhoist Quarry site contains vertical quarry faces of Cambrian-Ordovician Ellenburger Group north of the

town of Marble Falls, Texas. Due to safety protocols, the fault orientations and geometries were exclusively characterized using 3D models from orthorectified photogrammetry captured by aerial drone. Drone work during the spring of 2017 resulted in the construction of 12 3D models (Figure 8a) with scans covering active and inactive quarry walls (i.e., some of the data collected no longer exist). Raw and interpreted images of some of the mapped quarry walls are shown in Figure 8b–8g. In total, 1149 fault segments have been interpreted from these 3D outcrop models. The Ellenburger beds dip gently toward the north following the regional descent into the FWB. Bold white lines highlight key marker beds that are offset by faults and fractures. The location of each outcrop image is highlighted in Figure 8a.

Similar to the subsurface data regions, faults interpreted from outcrop models dominantly trend toward the northeast, with a mean strike of 025° (Figure 8h). Fault segments are generally planar with dips that range between 60° and 80° and a mean dip of 71.9° , broadly similar to the data set from Hoover Point. All faults with recognizable marker beds display a normal offset. Although the lateral length of the faults cannot be determined from these data, given the large dispersion in fault strike as shown in Figure 8h, it can also be postulated with confidence that the faults comprise an interconnected network in 3D.

Summary of outcrop interpretation domains

In total, 1410 fault segments have been interpreted from the Lhoist Quarry and Hoover Point 3D outcrop models. Faults dominantly strike toward the northeast, with a mean dip of 72° . The Hoover Point outcrop is structurally heterogeneous due to the changing mechanical properties of the Cambrian units, proximity to regional fault systems, and other factors that are beyond the scope of this research. Faults characterized from the Lhoist Quarry are especially useful because they occur within the Ellenburger Group, which is laterally equivalent to the subsurface interval most commonly targeted for SWD in the FWB. Both outcrop domains provide tangible evidence for how faulted and fractured the subsurface Ellenburger may be, and more importantly, that there is consistency in the fault dip from the outcrop and as interpreted using high-confidence subsurface data sets.

Integrated field and subsurface modeling

With all subsurface interpretation domains considered (ID1–4), 343 fault segments have been identified, verified, and integrated to generate the 3D framework of the subsurface FWB. Fault strikes are generally well constrained for each fault family (faults grouped by region or data used for interpretation) in this analysis; however, fault dips are less certain and have been estimated where appropriate. For example, fault interpretations

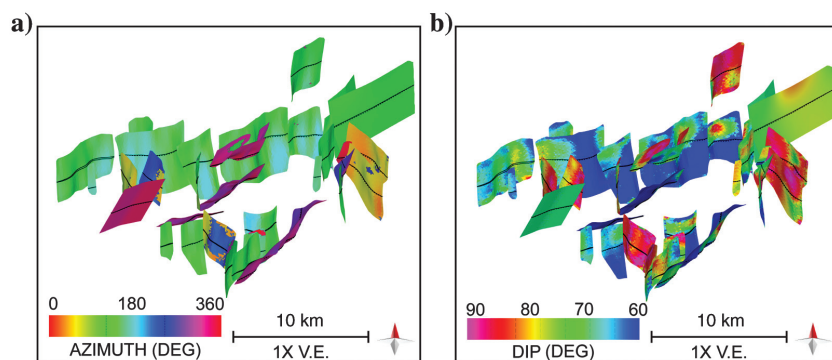


Figure 11. Oblique views of the 3D fault framework model of the 3D seismic (Venus) fault set. (a) Variability in azimuth (dip direction). (b) The dip angles are mapped on the fault surfaces. These images provide insight into potential complexities within other subsurface faults within the FWB. Faults range in height from 0.5 to 4 km.

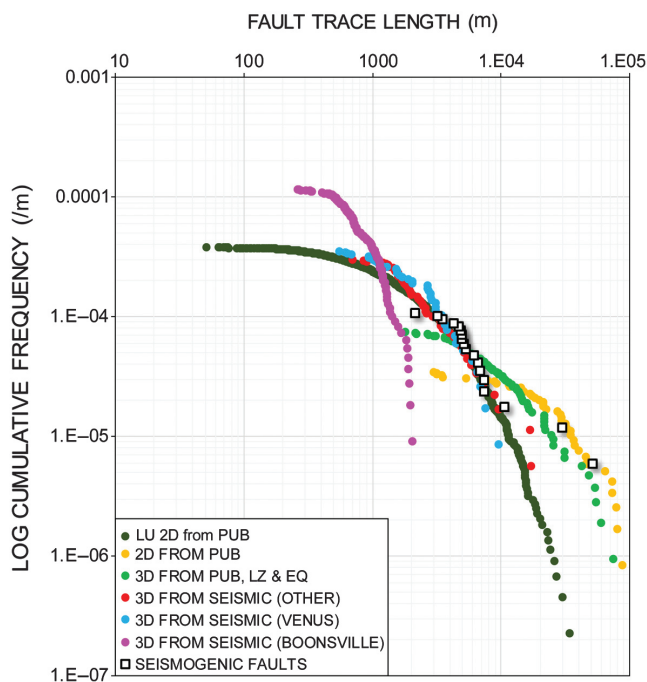


Figure 12. Cumulative frequency of the fault trace length plot, with data points colored by fault family.

from reflection seismic data and reliable earthquake hypocentral events provide a 3D context for nearby segments that lack 3D control. Orientations from faults interpreted from outcrop ($n = 1410$) and high-confidence subsurface data sets ($n = 88$) have been combined to generate 3D surfaces along segments with insufficient control. Specifically, earthquake hypocenters have defined the planes of 15 subsurface faults, which produced a mean dip of 67.8° . There are three faults in the Azle earthquake sequence, four faults near the town of Cleburne, four faults near the Irving-Dallas metropolis, two faults near Lake Lewisville, and two faults within the Venus sequence (Figure 2). Observations from the Hoover Point and Lhoist outcrops indicate that the faults have a generally consistent northeast strike and a mean dip of 72° . Therefore, a mean fault dip of 72° has been applied to 2D fault segments and 3D surfaces in the subsurface that otherwise lack dip constraint.

Using this mean dip value when constructing 3D fault surfaces from 2D constraints (i.e., fault traces from a single stratigraphic datum) produces faults for ID1 and ID2 that have planar, rather than curved or listric, surface geometries (Figure 5b and 5c). Fault segments interpreted from more robust subsurface data sets (ID3 and ID4) have more surface variation, with dip angles that change along strike and in some cases, decrease with depth (e.g., Figure 5d shows the listric geometry of the seismogenic fault named Venus [V] in the ID4b region).

Structural characterization 3D fault framework model

A 3D structural model of the FWB has been generated using all relevant data as previously discussed. The subsurface fault system is composed of 343 fault segments that generally trend to the northeast, creating a series of low-relief horsts and grabens (Figure 2). All segments are interpreted to root into the Precambrian basement and extend vertically into the Paleozoic succession (Figure 3b). For descriptive and analytical purposes, this subsurface fault array has been split into five fault families, named according to the data source: (1) 2D PUB, (2) 3D PUB, LZ, and EQ, (3) 3D SEISMIC (OTHER), (4) 3D SEISMIC (VENUS), and (5) 3D SEISMIC (BOONSVILLE). All of the fault segment surfaces are displayed in Figure 9. The source data information for each fault family has been outlined in Table 2. The number of segments within a fault family and their structural attributes, such as orientation (strike, dip), length,

throw, and confidence in interpretation, have been tabulated in Table 3 to assist in the descriptions.

Strike and dip

Fault segment geometries within the FWB faulted framework and outcropping LU are displayed as rose diagrams in Figure 10a–10i and are summarized in Table 3. Fault segments dominantly strike northeast–southwest, with an average dip of 72° . A secondary northwest–southeast fault strike can be observed in several fault families, but it is the dominant orientation for the 3D SEISMIC (BOONSVILLE) fault family (Figure 10e). In general, fault families that use 3D data to delineate faults result in more variation in strike and dip orientations. For instance, the 3D SEISMIC (VENUS) fault family

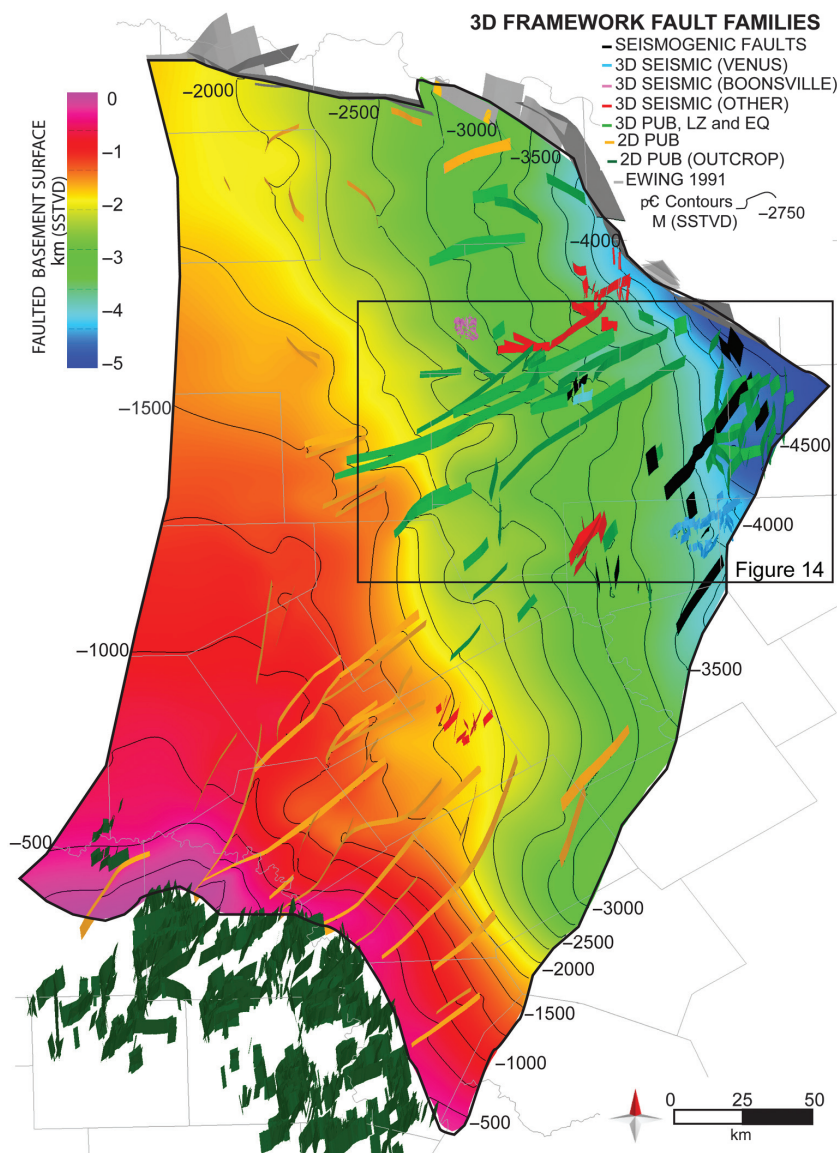


Figure 13. Oblique view of the constructed 3D faulted framework of the greater FWB. Fault segment surfaces are colored depending on their associated fault family, vertical heights generally range from 1.5 to 5 km, and the top of basement surface has been colored to reflect depth in meters subsea true vertical depth (SSTVD). Seismogenic fault segments are colored black.

exhibits significant variation in dip angle, with many segments' dip angles shallowing with depth (Figure 11a and 11b).

Trace length analysis

Fault segments within the subsurface faulted framework model range in length from 0.25 to 136 km. There is significant bias in this interpretation created by differences in control data density and resolution. This bias necessitates the independent assessment of the structural character for faults within each fault family, rather than as a whole. The mean and range of length values for each fault family have been tabulated in Table 3. The fault family with the greatest average length is the 2D PUBS, and the family with the shortest average length is 3D SEISMIC (BOONSVILLE). The cumulative frequency of fault trace lengths for each fault family is shown in Figure 12, highlighting the overlap in horizontal length between all FWB fault families, interpreted earthquake faults, and surficially mapped LU faults. Due to limitations in lateral exposure, fault segments interpreted from orthorectified 3D outcrop models from Hoover Point and Lhoist Quarry are omitted from this analysis.

Faulted basement surface

A 3D gridded surface of the top of Precambrian crystalline basement has been interpreted as part of the fault framework interpretation process using 2D and 3D data sets and will top correlations (Figure 13). In general, the FWB deepens toward the northeast and is deepest adjacent to the Muenster Arch and Ouachita thrust fronts. Faults generate considerable relief along the basement surface, with the most being generated by eastward-dipping faults. Figure 14 displays the basement surface

without the intersecting fault segment surfaces and highlights the horizontal displacement (heave) along faults in the northeastern portion of the FWB. The solid black lines on the basement-sediment interface indicate the upthrown footwall, and the dashed lines indicate the downthrown hanging wall.

Throw distribution

To characterize the distribution of displacement, we determined the fault throw versus length (T-L) for each fault family data set offsetting the basement-sediment interface. The regional distribution of fault throw at the basement-sediment interface is modeled in Figure 15a. In general, and as expected, the faults have the greatest amount of throw in the lateral center of the fault surface. This distribution can be observed in the Venus region (Figure 15b). Fault throws are greatest in the northern FWB, concentrated in SW Wise County, Tarrant County, and Dallas County (Figure 14). In some instances of linked-fault segments, maximum throw occurs at the fault segment linkage zone. Maxima, minima, and mean fault throw values for each fault family are summarized in Table 3. The confidence in each fault throw measurement is directly tied to the level of confidence assigned to the fault segment reflecting its respective source. Maximum throw (T) has been plot against segment length (L) to better understand growth histories. Each of these T-L analyses has been included in Figure 16. Fault segments with lengths greater than 15 km have disproportionately small throws and are considered underdisplaced.

Fault intensity

We use profiles through the 3D fault model to investigate if there are regional variations in the spacing of faults that may reflect original controls on the fault location and fault growth processes (Figure 17). The locations for these cross section profiles are highlighted in Figure 2. Section A is a regional transect that trends toward the east through the northern FWB (Figure 17a). This profile captures the regional tilt toward the east and intersects several basement-rooting normal faults that have been interpreted and validated in this study and by Hennings et al. (2019). Proximal earthquake hypocentral locations have been projected normal to the section and delineate their respective hosting fault planes. The midpoint distance between adjacent faults along section A has been calculated as a proxy for deformation intensity (Figure 17b). In general, faulting is concentrated in the east, with an average spacing of less than 5 km. After the most proximal 25 km, there is an extensive, approximately 30 km gap between fault segments, before picking up again in the west. Section B illustrates the subsurface projection of

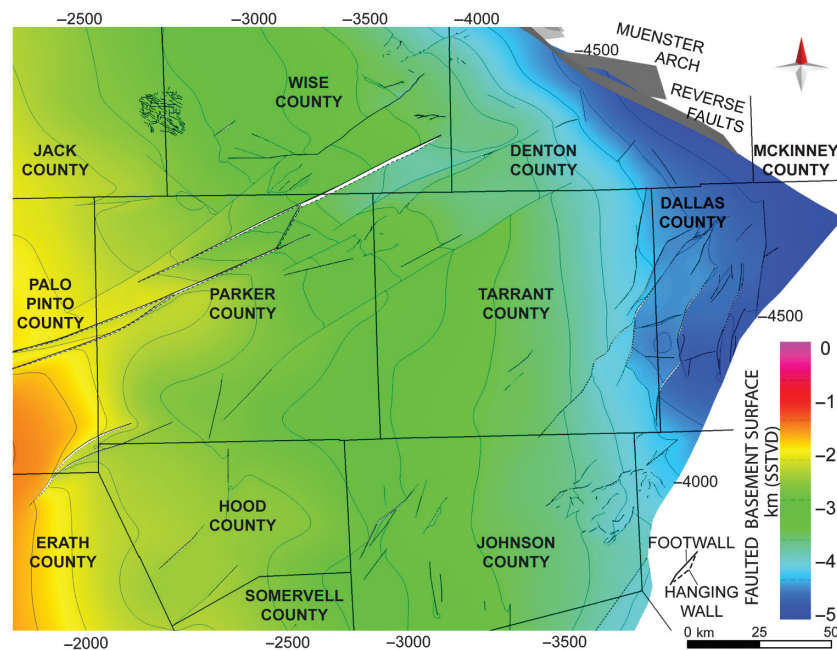


Figure 14. Inset map of the faulted basement-sediment interface in the northern FWB. The inset outline is shown in Figure 13.

outcropping regional faults along the northern margin of the LU (Figure 17c). Although faulting is more concentrated along this profile, there is a notable decrease in fault spacing toward the Ouachita thrust front in the east (Figure 17d). Section B captures the deformation intensity and structural style that is assumed to be present in the subsurface.

Characterization of seismogenic faults

Of the 343 faults included in our subsurface interpretation, only 18 (approximately 5%) have slipped recently and produced earthquakes. For each of the 10 named earthquake sequences in the FWB, there are 18 segments that are interpreted to have hosted earthquakes (Figure 18). Specifically, there are three mapped faults associated with the Azle-Reno sequence, four near the town of Cleburne, two associated with the Fort Worth City sequence, as many as four that have hosted the Irving-Dallas sequence, potentially two associated with the Lake Lewisville sequence, one associated with the activity near Grandview, Texas, and finally, possibly two faults that hosted activity as part of the Venus seismogenic sequence. This group of faults will be referred to as the earthquake fault set (Table 3), and is generally categorized as part of the 3D from LZ & EQ and the 3D SEISMIC (VENUS) fault families.

The average strike for the seismogenic faults also follows the regional primary orientation of northeast-trending strikes, with an average dip of approximately 72° (Table 3, Figure 19). In general, the fault length of seismogenic faults is less than 8 km, with the exception of the DFW fault segment, whose length is more than 50 km. Similarly, length-to-throw ratios for this fault set follow the overall cluster of 3D framework faults (Figure 16).

Additionally, the year of each earthquake event in the FWB has been tabulated and assigned to interpreted earthquake-hosting fault segment surfaces. This analysis enables the observable changes in frequency of earthquake events for each fault zone between the years (Table 4). Colored boxes signify the years that associated faults segments slipped, given the spatial relationship to well-located earthquake hypocenters. Lighter colors represent increasing or decreasing (intermittent) levels of seismicity, with richer colors reflecting years of more activity.

Discussion

Sampling bias and data impact

Our FWB subsurface data set is aerially extensive, yet faults are unevenly distributed. The most trusted data sets cover 1500 km² (approximately 2.4%) of the total area (ID3 and ID4, Figure 4). In these regions, we are confident that most of the faults with trace lengths greater than approximately 0.5 km have been identified, all of which root down through Paleozoic sediments and into crystalline basement. Data regions with lower

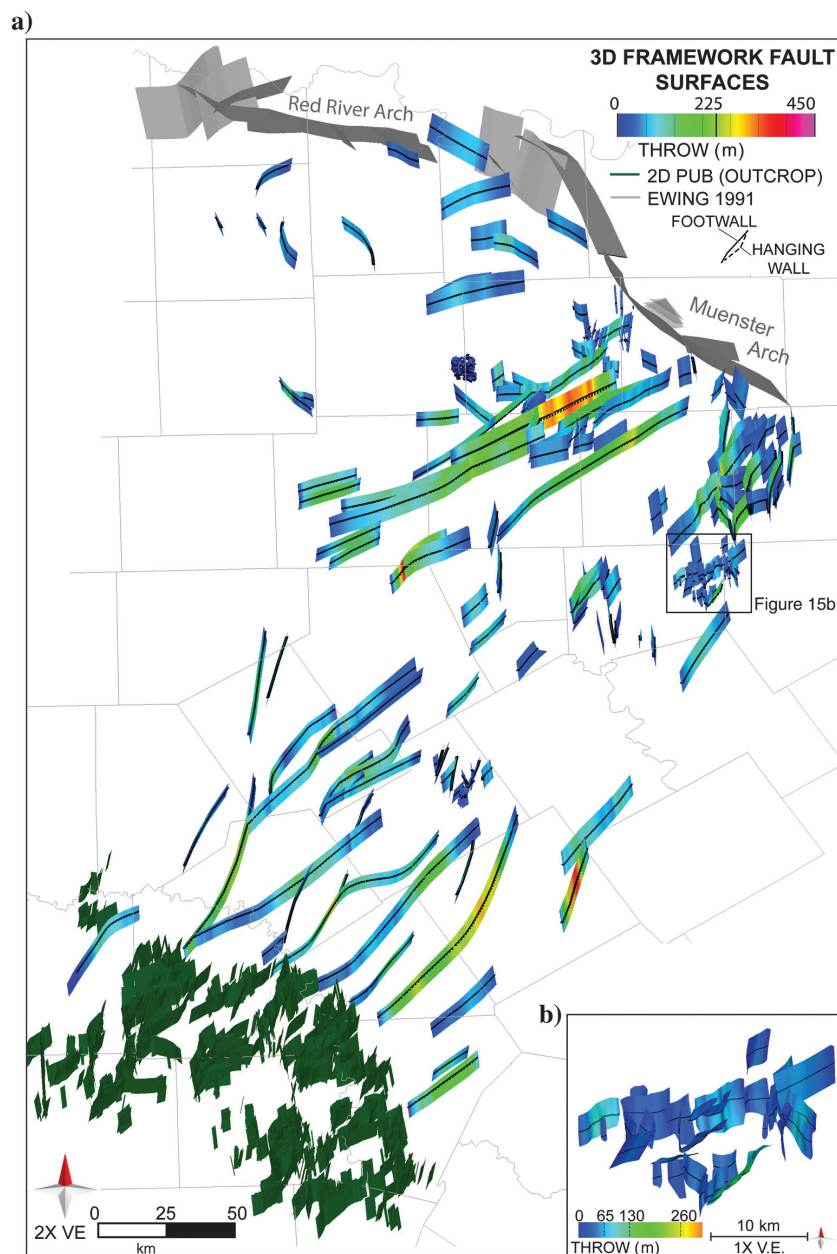


Figure 15. Oblique view north of the fault segment surfaces showing the fault throw along the basement-sediment interface within the (a) FWB and (b) 3D seismic (Venus) fault array. Fault surfaces are colored by variations in throw, and heights generally range from 1.5 to 5 km; the lines of intersection for the top Precambrian basement and the fault segment surface are shown as solid and dashed black polylines, reflecting the footwall and hanging-wall intersections, respectively.

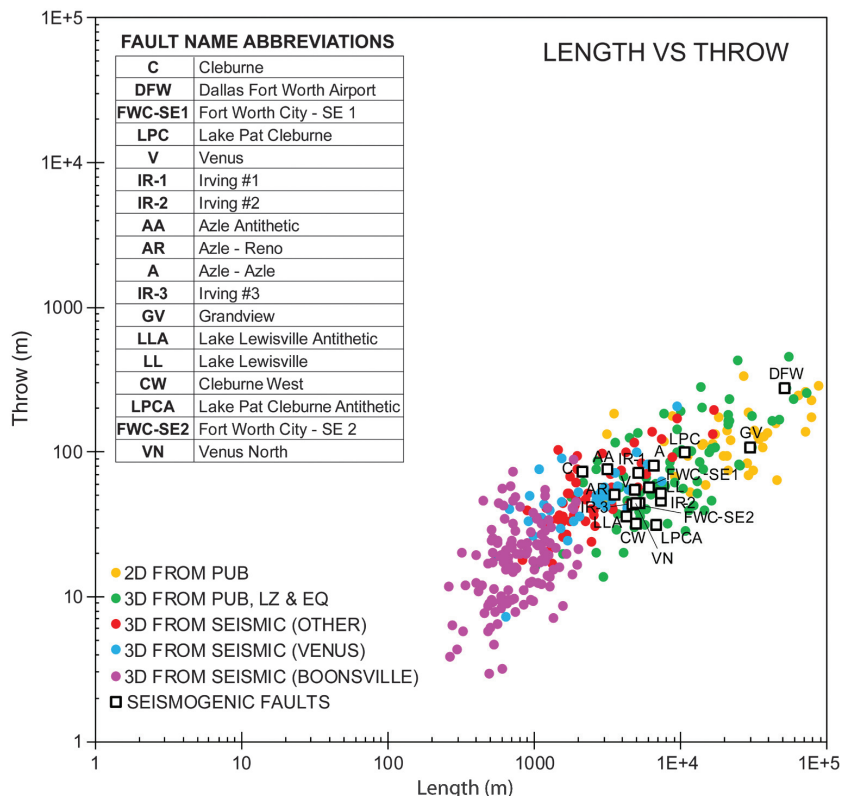


Figure 16. Length versus throw for subsurface faults in the FWB. Data points are colored by fault family, and known seismogenic faults are shown as the outlined black squares.

resolution, ID1 and ID2, have fault control information that is often interpolated laterally across significant distances. For these areas, we are confident that a majority of faults with trace lengths of greater than 5 km have been accounted for. Faults interpreted within data region ID2 use horizontal legs of production wells targeting the Barnett Shale; the vertical displacement of these horizontal legs is therefore interpreted to be minimum displacement thresholds, and it is assumed that these fault segments are all basement rooting, though we have little to no data to constrain the extent of each segments depth. Data from our field observations and orthorectified 3D outcrop models along the northeastern LU provide additional context for the degree of fine-scale deformation that may be present throughout the basin.

Due to the nature of the uneven quality of data, faults with greater lengths are controlled by sparse data sets and were inherited from previously published interpretations inferred from 2D seismic and wellbore data (e.g., Ewing, 1991). Such data sets validate the trend of the fault traces in the FWB, but in many

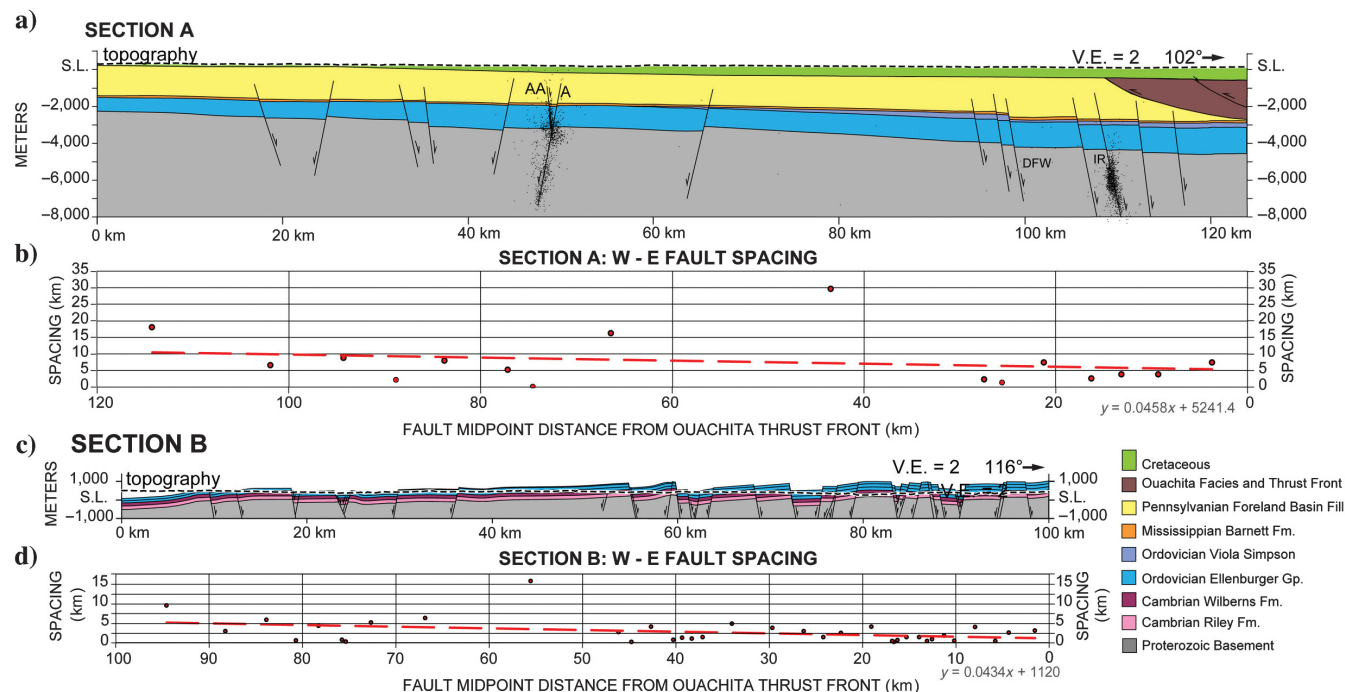


Figure 17. Cross sections from the FWB (section A) and LU (section B) illustrating the structural style and fault intensity (spacing). The section locations are specified in Figure 2. In the fault spacing plots, each point is midway between adjacent faults and referenced as the distance from the Ouachita thrust front.

cases, fault segments with lengths greater than 10 km are relatively underdisplaced, as their traces are overlong relative to their vertical displacement (e.g., [Schultz et al., 2008](#)). This underdisplacement may be due to the fact that these segment interpretations are more likely composed of several en echelon or subparallel relaying fault segments that may be hard- or soft-linked.

Basin-scale fault characteristics

The FWB appears to have faults of similar characteristics throughout. The faults have a normal offset, are rooted into the crystalline basement, and strike to the northeast, parallel to the bounding thrust front, and dip 72° from horizontal. These characteristics are observable in outcrop along the northern margin of the LU. Regional cross section profiles have been generated, resulting in the observation that the number of faults and relative deformation of faults increase toward the Ouachita thrust front (Figure 17). This increase in intensity is commonly observed in similar flexural foreland basins (e.g., [Bradley and Kidd, 1991](#)). It is likely that the distribution and character of the basement-rooting normal faults could also be attributed to Late Proterozoic and Cambrian rift events through tectonic inheritance because the rift margin is roughly parallel to the axis of the basin, the strike of the Ouachita thrust front, and most of the basement-rooting faults within the FWB. Although our controlling data vary in vintage, quality, and spatial sampling, the data presented here provide strong evidence that these fault geometries remain consistent in 3D character across the basin, but the fault throw is not observed to follow any discernible pattern.

Application to seismicity hazard assessment

Assessment of static characteristics shows similar, nonunique relationships between the total modeled fault population within the FWB and interpreted seismogenic faults. Figures 20 and 21 show histograms that compare the characteristics of the seismogenic faults and the total fault population. Fault segment surfaces have been resampled to have 200 m gridded cells, enabling static structural characterization of fault strike, dip, trace length, and throw. Between these fault data sets, there is a dominant northeast strike, which is consistent between data sets (Figure 19a and 19b). Additionally, there is very little variation in dip, (Figure 19c and 19d). This consistency is reflecting a bias introduced in our modeling

methods, in which fault segment traces with limited constraint on dip were projected into surfaces at a 72° dip. Seismogenic fault segments are generally less than 10 km in length, with the exception of the DFW fault (Figure 19e and 19f). Variations in throw measurements are displayed in Figure 21, showing the throw characteristic of the seismogenic faults relative to that of the overall fault population. These histograms make it clear that there is consistency between the modal distribution of the overall fault population and the seismogenic segments of the population.

Relevance to SWD-caused seismicity elsewhere in the midcontinent

There have been numerous studies linking wastewater injection to recent seismicity in the central and

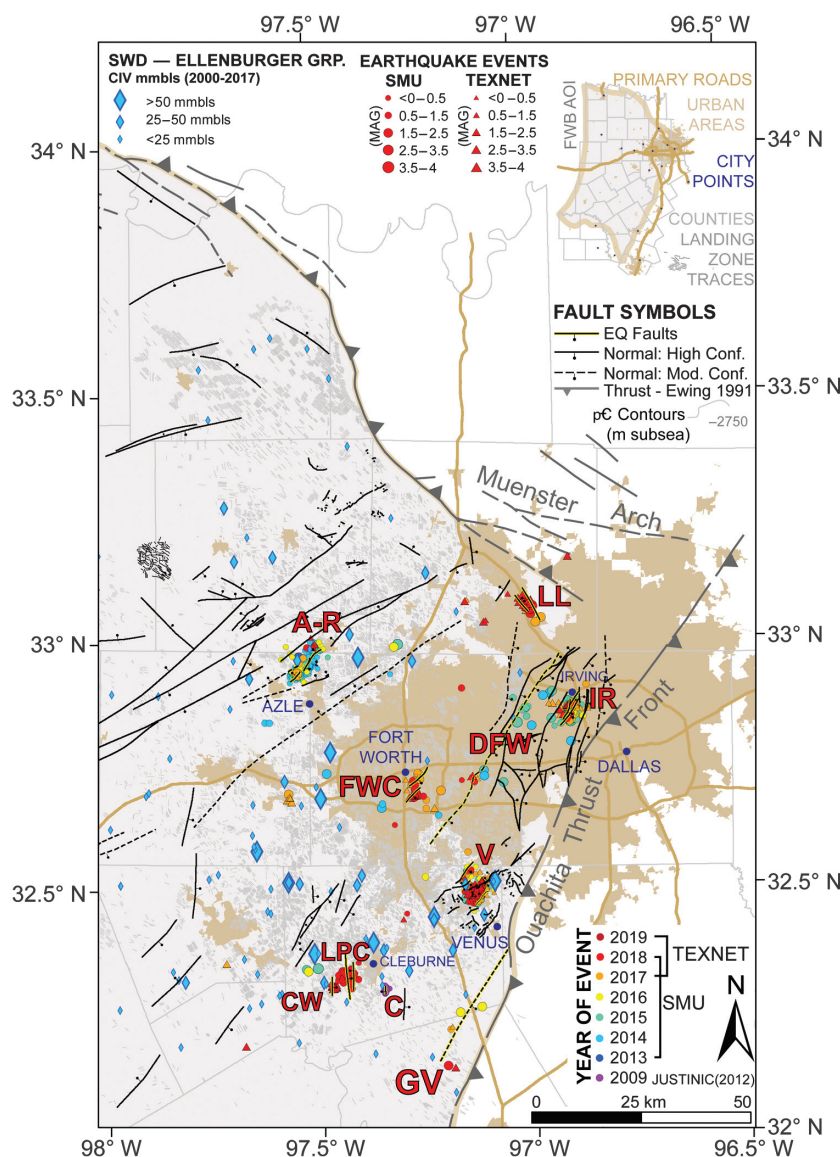


Figure 18. Inset map of the northeastern FWB showing high- and moderate-confidence faults. Seismogenic fault areas have been labeled: A-R, Azle-Reno; FWC, Fort Worth City; CW, Cleburne West; LPC, Lake Pat Cleburne; C, Cleburne; V, Venus; DFWA, Dallas-Fort Worth Airport; IR, Irving; LL, Lake Lewisville.

eastern United States (e.g., McGarr et al., 2002; Horton, 2012; Ellsworth, 2013; Kim, 2013; Buchanan, 2015; Schwab et al., 2017; Shah and Keller, 2017). In many cases, this seismicity can be spatially and temporally linked to wastewater injection into deep stratigraphic or crystalline basement intervals near preexisting faults (Ellsworth, 2013; Walsh and Zoback, 2015; Weingarten et al., 2015; Schwab et al., 2017).

The regional stress state, magnitude, and spatial extent of pore-pressure change, and subsurface architecture (lithologic properties and the presence and nature of preexisting faults) determine the probability for injection-induced earthquakes (Ellsworth, 2013; Weingarten et al., 2015). In particular, it is of great importance to determine if there is a preexisting fault fabric and if given the ambient stress conditions, if this system is well oriented for reactivation, or if there is a threshold for pore-pressure variation needed to induce reactivation (Zoback, 2012; Ellsworth, 2013; Huang et al., 2017; Hennings et al., 2019).

In Youngstown, Ohio, a series of low-magnitude (M_w 0.0–3.9) earthquakes have been determined to be triggered by increased pore pressure along preexisting subsurface faults close to SWD wells (Kim, 2013). We believe that this geologic system has important similarities to our work presented here including SWD reservoir intervals targeting Paleozoic dolomite and sandstone layers, which are in hydraulic connectivity with preexisting basement-rooted faults. In this region, all earthquake events have been located exclusively within the Precambrian basement, and fault plane solutions show that these triggered events caused strike-slip fault reactivation on well-oriented faults

(e.g., Nicholson et al., 1988; Zoback and Zoback, 1989; Baranoski, 2002; Du et al., 2003; Seeber et al., 2004; Kim, 2013).

In north-central Oklahoma, there have been a few instances of SWD-induced earthquakes with moderate magnitudes ($M_w \geq 5.0$) and over 6200 events with $M_w \geq 3.0$ for the period 2010–2018 (Kolawole et al., 2019). These events have primarily occurred on unmapped basement-rooted fault segments (McNamara et al., 2015). Similar to the events in Ohio, the preexisting faults in Oklahoma are critically stressed for strike-slip motion and are extremely sensitive to pore-pressure perturbations (Walsh and Zoback, 2016; Barbour et al., 2017; Kolawole et al., 2019). Research conducted by Kolawole

Table 4. Year of activity of the seismogenic faults as shown in Figure 19.

EQ sequence — fault	Abbreviation	2008	2009	2013	2014	2015	2016	2017	2018	2019
Azle — Azle	A									
Azle — Reno	AR					Mw 3.5				
Azle — Antithetic	AA									
Cleburne — Justinic 2012	C									
Cleburne — West	CW									
Dallas Fort Worth Airport	DFWA					Mw 3.6				
Fort Worth City — SE1	FWC-SE1									
Fort Worth City — SE2	FWC-SE2									
Grandview	GV									
Irving — #1	IR-1									
Irving — #2	IR-2					Mw 3.5				
Irving — #3	IR-3									
Lake Lewisville — Main	LL									
Lake Lewisville — Antithetic	LLA									
Lake Pat Cleburne — Main	LPC									
Lake Pat Cleburne — Antithetic	LPCA									
Venus — Main	V					Mw 4.0				
Venus — North	VN									

Note: Colored boxes signify years that these fault segments are interpreted to have slipped, given the spatial relationship to well-located earthquake hypocenters. Lighter colors represent increasing or decreasing (intermittent) levels of seismicity, with richer colors reflecting more active years (e.g., the Grandview sequence was active in 2016, with decreased levels of seismicity in 2017 and 2018).

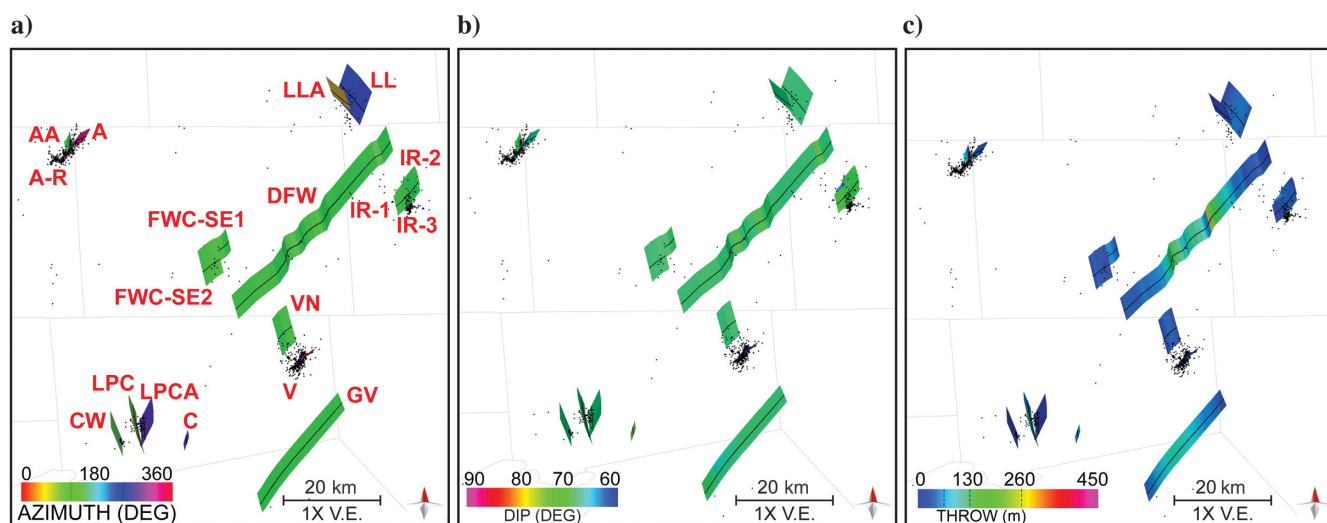


Figure 19. Oblique view of the 3D faulted framework for the seismogenic faults: (a) fault strike, (b) dip, and (c) throw. Fault segment abbreviations are labeled in (a) and are not vertically exaggerated.

et al. (2019) emphasizes the relationship between basement fabric and recent seismicity in Oklahoma, specifically that preexisting faults are critically stressed and can be reactivated under unfavorably oriented stresses as well as after long periods of tectonic quiescence. This

is similar to that observed in the FWB; however, preexisting fault segments are reactivating under normal faulting conditions rather than strike-slip, a product of the basin's stress state (e.g., Hennings et al., 2019). In Ohio and Oklahoma, well-located high-density earthquake

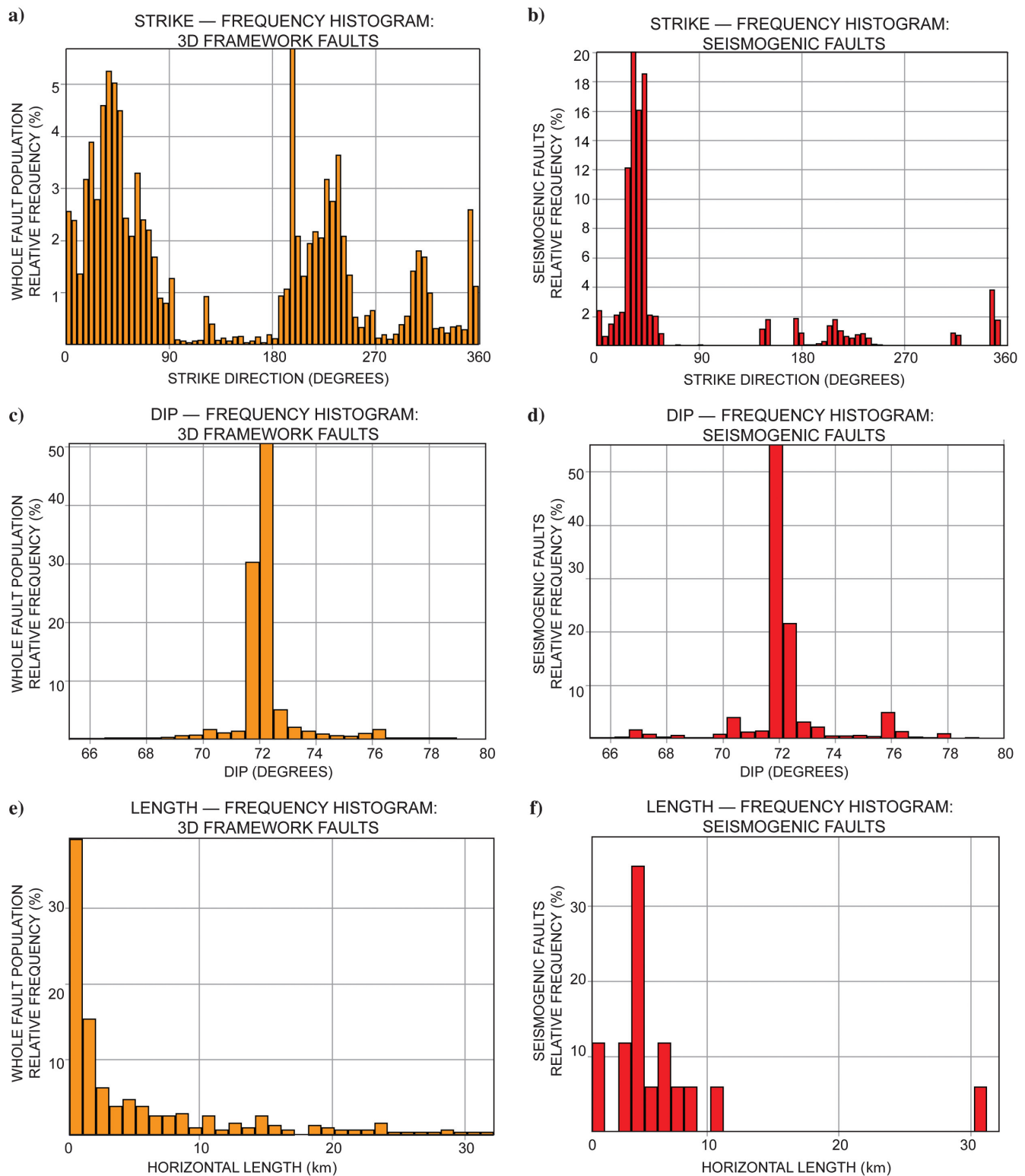


Figure 20. Relative frequency histograms of characteristics of the 3D faults and the seismogenic faults in the FWB.

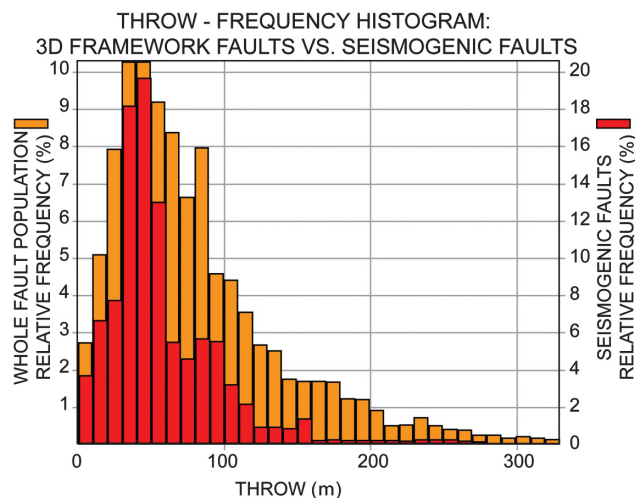


Figure 21. Relative frequency histograms of fault throw for the entire 3D fault population and the seismogenic faults.

hypocenter clusters have been used to delineate traces of reactivated faults (Fielding et al., 2017; Kolawole et al., 2019), a method used in the FWB by the authors.

Recommendations for future work

Results from this research can now be applied directly to a variety of future quantitative analyses in the FWB. Future earthquake events can be compared spatially to this interpretation for structural context. The 3D faulted framework can be used as a foundation for further geologic studies of the basin. The faults can be used regionally or locally as controls for permeability pathways and to generate discrete fracture network models as input to hydrogeologic models. The faults can also be used as the input to geomechanical modeling of earthquake processes.

Recent work conducted by Hennings et al. (2019) has resulted in the generation of an updated stress field and potentially seismogenic fault maps of the FWB region. When combined, these data sets can be used to probabilistically assess the FSP. Results from this previous research suggest that known seismogenic faults have the same probability of slip as a majority of other proposed faults in the basin. We recommend the direct application of the results of this study to a variety of research to reassess FSP because the number of interpreted faults within the basin has increased and the 3D geometries of the faults have been refined following both 3D reflection seismic interpretations, 3D outcrop models, and through the integration of well-located earthquake hypocenters.

Conclusions

The FWB is remarkably faulted. A vast multidisciplinary data set has been compiled to generate a 3D faulted framework. Newly interpreted and validated fault segment interpretations have been statically characterized. Earthquakes have occurred on basement-rooted normal

faults, primarily below the basement-sediment interface. Faults strike northeast–southwest with a mean strike orientation of 037° and dips that range $\pm 60^\circ$ from 70° . With the exception of the Lake Lewisville faults, Cleburne West and Lake Pat Cleburne seismogenic fault segments, the interpreted seismogenic faults follow the northeast–southwest fault trend. Statistical analysis of fault spacing, length, and throw show that faulting occurs at all scales within the basin and that the model is affected by a significant bias in spatial sampling. Fault intensity (faults/km) increases toward the Ouachita thrust front and Muenster Arch. Fault segments mapped within the 3D faulted framework range in trace length from 0.5 to 80 km, and seismogenic faults are generally less than 10 km in length. Fault traces that are greater than 15 km long are derived from sparse data sources. Fault throws range from 5 to 450 m. Fault segments with lengths greater than 15 km length are considered under-displaced. Increased access to higher resolution data sets (i.e., 3D seismic) basin-wide may provide clarity to this observed underdisplacement because many of the long fault traces may in reality be composed of a series of subparallel soft- and hard-linked normal fault relay zones. Outcropping faults in the LU are genetically related to subsurface faults. Outcrop fault models along the southern margin of the FWB show the potential deformation intensity that can be assumed to be typically present in the subsurface and their geometries help inform fault modeling in the FWB. Based on this analysis, there are no obvious structural characteristics differentiating the seismogenic faults from the total fault population. This implies that a significant percentage of the total population of faults may be susceptible to reactivation and seismicity as those that have slipped recently, agreeing with recent work done in the basin.

Data and Resources

The fault interpretation and characterization were performed by integrating published data, publicly available data, well data as interpreted from the IHS Markit database under an academic license, and fault data from proprietary 3D reflection seismic data as interpreted or verified by the authors. Faults interpreted in the northeastern portion of area ID2 used map and cross section interpretations and data publicly available from the Railroad Commission of Texas Hearing Docket 09-0296411. Faults within ID4a were interpreted by the authors on the Boonsville 3D Seismic Data Set that can be obtained at Hardage et al. (1996c). Faults for areas ID3a and ID4b come from fault data provided by petroleum operators using proprietary seismic data. A geographic information system shapefile and a layer file for the subsurface fault trace interpretations are publicly available within the Texas Data Repository (Horne, 2020). The TexNet Earthquake Catalog is available at TexNet Earthquake Catalog (2019). US Geological Survey (USGS) Advanced National Seismic System Comprehensive Catalog (ComCat) is available at United States Geological Survey (USGS) (2018).

Acknowledgments

We thank XTO and ConocoPhillips for access to proprietary fault information from 3D reflection seismic data. We thank IHS Markit for access to well databases and Petra software, Schlumberger for access to the Petrel E&P Software Platform, Badley Geoscience Ltd. for access to T7 software, and Petroleum Experts/Midland Valley for access to Move software. This work was supported by the state of Texas through the University of Texas Bureau of Economic Geology TexNet Seismic Monitoring and Research Project, and the industrial affiliates of the Center for Integrated Seismicity Research. The authors thank the three anonymous reviewers and the associate editor B. Carpenter for feedback and suggestions that greatly enhanced the manuscript.

Data and materials availability

Data associated with this research are available and can be accessed via the following URL: <https://doi.org/10.18738/T8/5EDCKC>.

References

- Aktepe, S., K. J. Marfurt, and R. Perez, 2008, Attribute expression of basement faulting — Time versus depth migration: *The Leading Edge*, **27**, 360–367, doi: [10.1190/1.2896627](https://doi.org/10.1190/1.2896627).
- Alhakeem, A. A., 2013, 3D seismic data interpretation of Boonsville Field, Texas: Master's thesis, Missouri University of Science and Technology.
- Alsalem, O. B., M. Fan, J. Zamora, X. Xie, and W. R. Griffin, 2017, Paleozoic sediment dispersal before and during the collision between Laurentia and Gondwana in the Fort Worth Basin, USA: *Geosphere*, **14**, 325–342, doi: [10.1130/GES01480.1](https://doi.org/10.1130/GES01480.1).
- Amsbury, D. L., and W. T. Haenggi, 1991, Middle Pennsylvanian strike-slip faulting on the eastern edge of the Llano Uplift, Central Texas: *Gulf Coast Association of Geological Societies Transactions*, **41**, 11–11.
- Amsbury, D. L., and W. T. Haenggi, 1993, Middle Pennsylvanian strike-slip faulting on the eastern edge of the Llano Uplift, Central Texas: *South Texas Geological Society Bulletin*, **34**, 9–16.
- Amsbury, D. L., R. Hickerson, and W. Haenggi, 1994, GCAGS guidebook: Fractures caused by north-south compression, eastern Llano Uplift, Central Texas: A field guide: *Gulf Coast Association of Geological Societies*.
- Ball, M. M., and W. J. Perry, 1996, Bend Arch-Fort Worth Basin Province (045), in D. L. Gautier, G. L. Dolton, K. I. Takahashi, and K. L. Varnes, eds., *National Assessment of United States Oil and Gas Resources — Results, Methodology, and Supporting Data: U.S. Geological Survey Digital Data Series DDS-30, Release 2, [CD-ROM]*, U.S. Geological Survey (USGS).
- Baranoski, M. T., 2002, tructure contour map on the Precambrian unconformity surface in Ohio and related basement features, report, Div. Geol. Surv. Map PG-23, scale 1:500,000, Ohio Department of Natural Resources, Columbus, <http://www.dnr.state.oh.us/Portals/10/pdf/mappg23.pdf>.
- Barbour, A. J., J. H. Norbeck, and J. L. Rubinstein, 2017, The effects of varying injection rates in Osage County, Oklahoma, on the 2016 M_w 5.8 Pawnee Earthquake: *Seismological Research Letters*, **88**, 1040–1053, doi: [10.1785/0220170003](https://doi.org/10.1785/0220170003).
- Barnes, V. E., 1982, Geology of the Pedernales Falls quadrangle, Blanco County, Texas: The University of Texas at Austin, Bureau of Economic Geology, Geologic Quadrangle Map, No. 49, map scale 1:24,000.
- Barnes, V. E., and W. C. Bell, 1977, The Moore Hollow Group of Central Texas: The University of Texas at Austin, Bureau of Economic Geology: Report of Investigations, **88**, 169, doi: [10.23867/RI0088D](https://doi.org/10.23867/RI0088D).
- Barnes, V. E., and P. R. Rose, 1981, Geological Atlas of Texas, Llano Sheet: The University of Texas at Austin, Bureau of Economic Geology, Geologic Atlas of Texas, map scale 1:250,000.
- Belforte, A. S., 1971, Pre-Canyon structural geology of the southern end of the Fort Worth Basin, Central Texas: Master's thesis, The University of Texas at Austin.
- Bell, W. C., and V. E. Barnes, 1972, Cambrian history, Llano region, in V. E. Barnes, W. C. Bell, S. E. Clabaugh, P. E. J. Cloud, R. V. McGehee, P. U. Rodda, and K. Young, eds., *Geology of the Llano Region and Austin Area, Guidebook: Bureau of Economic Geology, The University of Texas at Austin*, 24–29.
- Bradley, D. C., and W. S. F. Kidd, 1991, Flexural extension of the upper continental crust in collisional foredeeps: *Geological Society of America Bulletin*, **103**, 1416–1438, doi: [10.1130/0016-7606\(1991\)103<1416:FEOTUC>2.3.CO;2](https://doi.org/10.1130/0016-7606(1991)103<1416:FEOTUC>2.3.CO;2).
- Bruner, K. R., and R. Smosna, 2011, A comparative study of the Mississippian Barnett Shale, Fort Worth Basin, and Devonian Marcellus Shale, Appalachian Basin: Technical Report DOE/NETL-2011/1478, National Energy Technology Laboratory (NETL) for the U.S. Department of Energy.
- Buchanan, R. C., 2015, Increased seismicity in Kansas: *The Leading Edge*, **34**, 614–617, doi: [10.1190/tle34060614.1](https://doi.org/10.1190/tle34060614.1).
- Carlson, W. D., 1998, Petrologic constraints on the tectonic evolution of the Llano Uplift, in J. P. Hogan and M. C. Gilbert, eds., *Basement tectonics 12: Springer*, 3–27.
- Carlson, W. D., and J. F. Reese, 1994, Nearly pure iron staurolite in the Llano Uplift and its petrologic significance: *American Mineralogist*, **79**, 154–160.
- Chen, R., X. Xue, C. Yao, A. Datta-Gupta, M. J. King, P. Hennings, and R. Dommissé, 2018, Coupled fluid flow and geomechanical modeling of seismicity in the Azle area North Texas: SPE Annual Technical Conference and Exhibition.
- Cloud, P. E., Jr., and V. E. Barnes, 1946, The Ellenburger Group of Central Texas: University of Texas, Publication No. 4621.
- DeShon, H. R., C. T. Hayward, P. O. Ogwari, L. Quinones, O. Sufri, B. Stump, and M. Beatrice Magnani, 2018, Summary of the north Texas earthquake study seismic

- networks, 2013–2018: *Seismological Research Letters*, **90**, 387–394, doi: [10.1785/0220180269](https://doi.org/10.1785/0220180269).
- Dommissive, R., 2013, 3-D geological interpretation examples in unconventional shale reservoirs: Unconventional Resources Technology Conference, 2308–2313.
- Dommissive, R., L. Sivila, F. Male, and H. S. Hamlin, 2018, The value of building a multiscale, regional geomodel for reserves assessment of the Midland Basin: Proceedings of the 6th Unconventional Resources Technology Conference, 2–11.
- Du, W. X., W. Y. Kim, and L. R. Sykes, 2003, Earthquake source parameters and state of stress for the northeastern United States and southeastern Canada from analysis of regional seismograms: *Bulletin of the Seismological Society of America*, **93**, 1633–1648, doi: [10.1785/0120020217](https://doi.org/10.1785/0120020217).
- Eastman, H. S., and T. Murin, 2016, NETL-TRS-17-2016: NETL Technical Report Series, U.S. Department of Energy, National Energy Technology Laboratory.
- Elebiju, O. O., G. R. Keller, and K. J. Marfurt, 2010, Investigation of links between Precambrian basement structure and Paleozoic strata in the Fort Worth Basin, Texas, U.S.A., using high-resolution aeromagnetic (HRAM) data and seismic attributes: *Geophysics*, **75**, no. 4, B157–B168, doi: [10.1190/1.3435939](https://doi.org/10.1190/1.3435939).
- Ellsworth, W. L., 2013, Injection-induced earthquakes: *Science*, **341**, 1225942, doi: [10.1126/science.1225942](https://doi.org/10.1126/science.1225942).
- Ewing, T. E., 1991, The tectonic framework of Texas: Text to accompany “The Tectonic Map of Texas”: The University of Texas at Austin, Bureau of Economic Geology, <http://www.worldcat.org/title/tectonic-framework-of-texas-text-to-accompany-the-tectonicmap-of-texas/oclc/24400900>, accessed January 2020.
- Fielding, E. J., S. S. Sangha, D. P. S. Bekaert, S. V. Samsonov, and J. C. Chang, 2017, Surface deformation of north-central Oklahoma related to the 2016 Mw 5.8 Pawnee Earthquake from SAR interferometry time series: *Seismological Research Letters*, **88**, 971–982, doi: [10.1785/0220170010](https://doi.org/10.1785/0220170010).
- Flawn, P. T., 1959, The Ouachita structural belt: The Geology of the Ouachita Mountains Symposium, 20–29.
- Freeman, T., and G. L. Wilde, 1964, Age and stratigraphic implications of a major fault in Llano region, Central Texas: *Bulletin of the American Association of Petroleum Geologists*, **48**, 714–718, doi: [10.1306/BC743D2B-16BE-11D7-8645000102C1865D](https://doi.org/10.1306/BC743D2B-16BE-11D7-8645000102C1865D).
- Frohlich, C., 2012, Two-year survey comparing earthquake activity and injection-well locations in the Barnett Shale, Texas: Proceedings of the National Academy of Sciences, **109**, 13934–13938, doi: [10.1073/pnas.1207728109](https://doi.org/10.1073/pnas.1207728109).
- Frohlich, C., C. Hayward, B. Stump, and E. Potter, 2011, The Dallas-Fort Worth earthquake sequence: October 2008 through May 2009: *Bulletin of the Seismological Society of America*, **101**, 327–340, doi: [10.1785/0120100131](https://doi.org/10.1785/0120100131).
- Frohlich, C., E. Potter, C. Hayward, and B. Stump, 2010, Dallas-Fort Worth earthquakes coincident with activity associated with natural gas production: The Leading Edge, **29**, 270–275, doi: [10.1190/1.3353720](https://doi.org/10.1190/1.3353720).
- George, M. C., 2016, The Meunster Uplift of north Texas: The easternmost expression of the Pennsylvanian Ancestral Rockies: Master’s thesis, The University of Texas at Dallas.
- Gono, V., J. E. Olson, and J. F. Gale, 2015, Understanding the correlation between induced seismicity and wastewater injection in the Fort Worth Basin: 49th US Rock Mechanics/Geomechanics Symposium, American Rock Mechanics Association, 15-00419.
- Hardage, B. A., 1996, Boonsville 3-D data set: The Leading Edge, **15**, 835–837, doi: [10.1190/1.1437376](https://doi.org/10.1190/1.1437376).
- Hardage, B. A., D. L. Carr, D. E. Lancaster, J. L. Simmons, R. Y. Elphick, V. M. Pendleton, and R. A. Johns, 1996a, 3-D seismic evidence of the effects of carbonate karst collapse on overlying clastic stratigraphy and reservoir compartmentalization: *Geophysics*, **61**, 1336–1350, doi: [10.1190/1.1444057](https://doi.org/10.1190/1.1444057).
- Hardage, B. A., D. L. Carr, D. E. Lancaster, J. L. Simmons, D. S. Hamilton, R. Y. Elphick, K. L. Oliver, and R. A. Johns, 1996b, 3-D seismic imaging and seismic attribute analysis of genetic sequences deposited in low-accommodation conditions: *Geophysics*, **61**, 1351–1362, doi: [10.1190/1.1444058](https://doi.org/10.1190/1.1444058).
- Hardage, B. A., J. L. Simmons, Jr., D. E. Lancaster, R. Y. Elphick, R. D. Edson, D. L. Carr, and V. Pendleton, 1996c, Boonsville 3-D Seismic Data Set, The University of Texas at Austin, Bureau of Economic Geology, SW 7, <https://store.beg.utexas.edu/cd-rom-sets/1311-sw0007.html>, accessed December 2019.
- Hatcher, R. D., W. A. Thomas, and G. W. Viele, 1989, The Appalachian-Ouachita Orogen in the United States: Geological Society of America.
- Hennings, P. H., J. Lund Snee, J. L. Osmond, H. R. DeShon, R. Dommissive, E. Horne, C. Lemons, and M. D. Zoback, 2019, Injection-induced seismicity and fault-slip potential in the Fort Worth Basin, Texas: *Bulletin of the Seismological Society of America*, **109**, 1615–1634, doi: [10.1785/0120190017](https://doi.org/10.1785/0120190017).
- Hentz, T. F., W. A. Ambrose, and D. L. Carr, 2012, Reservoir systems of the Pennsylvanian Lower Atoka Group (Bend Conglomerate), northern Fort Worth Basin, Texas: High-resolution facies distribution, structural controls on sedimentation, and production trends: *AAPG Bulletin*, **96**, 1301–1332, doi: [10.1306/10041111078](https://doi.org/10.1306/10041111078).
- Horne, E. A., 2020, Fault Trace Data for: Horne et al., 2020, Structural characterization of potentially seismogenic faults in the Fort Worth Basin: Texas Data Repository Dataverse, V1, doi: [10.18738/TS/5EDCKC](https://doi.org/10.18738/TS/5EDCKC).
- Hornbach, M. J., H. R. DeShon, W. L. Ellsworth, B. W. Stump, C. Hayward, C. Frohlich, H. R. Oldham, J. E. Olson, M. B. Magnani, C. Brokaw, and J. H. Luetgert, 2015, Causal factors for seismicity near Azle, Texas: *Nature Communications*, **6**, 1–11, doi: [10.1038/ncomms7728](https://doi.org/10.1038/ncomms7728).

- Hornbach, M. J., M. Jones, M. Scales, H. R. DeShon, M. B. Magnani, C. Frohlich, B. Stump, C. Hayward, and M. Layton, 2016, Ellenburger wastewater injection and seismicity in north Texas: *Physics of the Earth and Planetary Interiors*, **261**, 54–68, doi: [10.1016/j.pepi.2016.06.012](https://doi.org/10.1016/j.pepi.2016.06.012).
- Horton, S., 2012, Disposal of hydrofracking waste fluid by injection into subsurface aquifers triggers earthquake swarm in central Arkansas with potential for damaging earthquake: *Seismological Research Letters*, **83**, 250–260, doi: [10.1785/gssrl.83.2.250](https://doi.org/10.1785/gssrl.83.2.250).
- Howe, A. M., 2012, Analysis of the Cleburne earthquake sequence from June 2009 to June 2010, Master's Thesis, Southern Methodist University, Dallas, Texas.
- Huang, Y., W. L. Ellsworth, and G. C. Beroza, 2017, Stress drops of induced and tectonic earthquakes in the central United States are indistinguishable: *Science Advances*, **3**, 7, doi: [10.1126/sciadv.1700772](https://doi.org/10.1126/sciadv.1700772).
- Ikonnikova, S., J. Browning, S. C. Horvath, and S. Tinker, 2014, Well recovery, drainage area, and future drill-well inventory: Empirical study of the Barnett Shale gas play: *SPE Reservoir Evaluation & Engineering*, **17**, 484–496, doi: [10.2118/171552-PA](https://doi.org/10.2118/171552-PA).
- Janská, E., and L. Eisner, 2012, Ongoing seismicity in the Dallas-Fort Worth area: The Leading Edge, **31**, 1462–1468, doi: [10.1190/tle31121462.1](https://doi.org/10.1190/tle31121462.1).
- Jarvie, D. M., R. J. Hill, T. E. Ruble, and R. M. Pollastro, 2007, Unconventional shale-gas systems: The Mississippian Barnett Shale of north-Central Texas as one model for thermogenic shale-gas assessment: *AAPG Bulletin*, **91**, 475–499, doi: [10.1306/12190606068](https://doi.org/10.1306/12190606068).
- Johnson, B., 2004, The Llano Uplift and associated Pennsylvanian-age faults: An overview and a field example of faults exposed at Hoover Point in the Backbone Ridge: *Austin Geological Society Field Trip Guidebook*.
- Justinic, A. H., B. Stump, C. Hayward, and C. Frohlich, 2013, Analysis of the Cleburne, Texas, earthquake sequence from June 2009 to June 2010: *Bulletin of the Seismological Society of America*, **103**, 3083–3093, doi: [10.1785/0120120336](https://doi.org/10.1785/0120120336).
- Khatiwada, M., G. R. Keller, and K. J. Marfurt, 2013, A window into the Proterozoic: Integrating 3D seismic, gravity, and magnetic data to image subbasement structures in the southeast Fort Worth Basin: *Interpretation*, **1**, no. 2, T125–T141, doi: [10.1190/INT-2013-0041.1](https://doi.org/10.1190/INT-2013-0041.1).
- Kier, R. S., 1988, Paleozoic strata of the Llano region, Central Texas, *in* O. T. Heyward, ed. *Centennial field guide: South-Central Section of the Geological Society of America* 4, 351–360.
- Kier, R. S., L. F. J. Brown, P. Harwood, and V. E. Barnes, 1976, *Geological Atlas of Texas, Brownwood Sheet: The University of Texas at Austin, Bureau of Economic Geology (GA0008, Scale 1:250,000)*.
- Kim, W. Y., 2013, Induced seismicity associated with fluid injection into a deep well in Youngstown, Ohio: *Journal of Geophysical Research: Solid Earth*, **118**, 3506–3518, doi: [10.1002/jgrb.50247](https://doi.org/10.1002/jgrb.50247).
- Kolawole, F., C. S. Johnston, C. B. Morgan, J. C. Chang, K. J. Marfurt, D. A. Lockner, Z. Reches, and B. M. Carpenter, 2019, The susceptibility of Oklahoma's basement to seismic reactivation: *Nature Geoscience*, **12**, 839–844, doi: [10.1038/s41561-019-0440-5](https://doi.org/10.1038/s41561-019-0440-5).
- Krantz, B., and T. G. Neely, 2016, Subsurface structural interpretation: The significance of 3-D structural frameworks, 3D structural interpretation: *Earth, mind, and machine: AAPG Memoir* 111, 91–109, doi: [10.1306/13561988M1113181](https://doi.org/10.1306/13561988M1113181).
- Leary, R. J., P. Umhoefer, M. E. Smith, and N. Riggs, 2017, A three-sided orogen: A new tectonic model for Ancestral Rocky Mountain uplift and basin development: *Geology*, **45**, 399–402, doi: [10.1130/G38830.1](https://doi.org/10.1130/G38830.1).
- Loucks, R., 2003, Review of the lower Ordovician Ellenburger Group of the Permian Basin, West Texas: Bureau of Economic Geology, The University of Texas at Austin, http://www.beg.utexas.edu/resprog/permianbasin/PBGSP_members/writ_synth/Ellenburger%20report.pdf, accessed January 2020.
- Lund Snee, J. E., and M. D. Zoback, 2016, State of stress in Texas: Implications for induced seismicity: *Geophysical Research Letters*, **43**, 10208–10214, doi: [10.1002/2016GL070974](https://doi.org/10.1002/2016GL070974).
- Magnani, M. B., M. L. Blanpied, H. R. DeShon, and M. J. Hornbach, 2017, Discriminating between natural versus induced seismicity from long-term deformation history of intraplate faults: *Science Advances*, **3**, e1701593, doi: [10.1126/sciadv.1701593](https://doi.org/10.1126/sciadv.1701593).
- McDonnell, A., R. G. Loucks, and T. Dooley, 2007, Quantifying the origin and geometry of circular sag structures in northern Fort Worth Basin, Texas: Paleocave collapse, pull-apart fault systems, or hydrothermal alteration? *AAPG Bulletin*, **91**, 1295–1318, doi: [10.1306/05170706086](https://doi.org/10.1306/05170706086).
- McGarr, A., D. Simpson, and L. Seeber, 2002, Case histories of induced and triggered seismicity: *International Geophysics*, **81**, 647–661, doi: [10.1016/S0074-6142\(02\)80243-1](https://doi.org/10.1016/S0074-6142(02)80243-1).
- McNamara, D. E., H. M. Benz, R. B. Herrmann, E. A. Bergman, P. Earle, A. Holland, R. Baldwin, and A. Gassner, 2015, Earthquake hypocenters and focal mechanisms in central Oklahoma reveal a complex system of reactivated subsurface strike-slip faulting: *Geophysical Research Letters*, **42**, 2742–2749, doi: [10.1002/2014GL062730](https://doi.org/10.1002/2014GL062730).
- Nicholas, R. L., and R. A. Rozendal, 1975, Subsurface positive elements within Ouachita foldbelt in Texas and their relation to Paleozoic cratonic margin: *AAPG Bulletin*, **59**, 193–216, doi: [10.1306/83D922D0-16C7-11D7-8645000102C1865D](https://doi.org/10.1306/83D922D0-16C7-11D7-8645000102C1865D).
- Nicholas, R. L., and D. E. Waddell, 1989, The Ouachita system in the subsurface of Texas, Arkansas, and Louisiana, *in* R. D. Hatcher, Jr., W. A. Thomas, and G. W. Viele, eds., *The Appalachian-Ouachita Orogen in the United States: the Geology of North America: Geologi-*

- cal Society of America, Boulder, Colorado, F-2, 661–672.
- Nicholson, C., E. Roeloffs, and R. L. Wesson, 1988, The northeastern Ohio earthquake of 31 January 1986: Was it induced? *Bulletin of the Seismological Society of America*, **78**, 188–217.
- Ogwari, P. O., H. R. DeShon, and M. J. Hornbach, 2018, The Dallas-Fort Worth airport earthquake sequence: Seismicity beyond injection period: *Journal of Geophysical Research: Solid Earth*, **123**, 553–563, doi: [10.1002/2017JB015003](https://doi.org/10.1002/2017JB015003).
- Paige, S., 1912, Description of the Llano and Burnet Quadrangles: U. S. Geological Survey, *Geologic Atlas Folio 183*.
- Patterson, A. A., 2010, Structural geology and hydrocarbon production, Barnett Shale (Mississippian), Fort Worth Basin, northwestern Johnson County, Texas: Master's thesis, Texas Christian University.
- Pollastro, R. M., D. M. Jarvie, R. J. Hill, and C. W. Adams, 2007, Geologic framework of the Mississippian Barnett Shale, Barnett-Paleozoic total petroleum system, Bend Arch-Fort Worth Basin, Texas: *AAPG Bulletin*, **91**, 405–436.
- Poole, F. G., W. J. Perry, R. J. Madrid, and R. Amaya-Martínez, 2017, Tectonics synthesis of the Ouachita-Marathon-Sonora orogenic margin of southern Laurentia: Stratigraphic and structural implications for timing of deformational events and plate-tectonic model, in T. H. Anderson, J. A. Nourse, J. W. McKee, and M. B. Steiner, eds., *The Mojave-Sonora megashear hypothesis: Development, assessment, and alternatives*: Geological Society of America Special Paper 393, 543–596.
- Qi, J., B. Zhang, H. Zhou, and K. Marfurt, 2014, Attribute expression of fault-controlled karst — Fort Worth Basin, Texas: A tutorial: *Interpretation*, **2**, no. 3, SF91–SF110, doi: [10.1190/INT-2013-0188.1](https://doi.org/10.1190/INT-2013-0188.1).
- Quinones, L., H. R. DeShon, S. Jeong, P. Ogwari, O. Sufri, M. M. Holt, and K. B. Kwong, 2019, Tracking induced seismicity in the Fort Worth Basin: A summary of the 2008–2018 north Texas earthquake study catalog: *Bulletin of the Seismological Society of America*, **109**, 1203–1216, doi: [10.1785/0120190057](https://doi.org/10.1785/0120190057).
- Quinones, L. A., H. R. DeShon, M. B. Magnani, and C. Frohlich, 2018, Stress orientations in the Fort Worth Basin, Texas, determined from earthquake focal mechanisms: *Bulletin of the Seismological Society of America*, **108**, 1124–1132, doi: [10.1785/0120170337](https://doi.org/10.1785/0120170337).
- Railroad Commission of Texas, 2016, <https://www.rrc.texas.gov/about-us/resourcecenter/research/online-research-queries/>, accessed February 2020.
- Reese, J. F., and S. Mosher, 2004, Kinematic constraints on Rodinia reconstructions from the core of the Texas Grenville Orogen: *The Journal of Geology*, **112**, 185–205, doi: [10.1086/381657](https://doi.org/10.1086/381657).
- Reese, J. F., S. Mosher, J. Connelly, and R. Roback, 2000, Mesoproterozoic chronostratigraphy of the southeastern Llano Uplift, Central Texas: *Geological Society of America Bulletin*, **112**, 278–291, doi: [10.1130/0016-7606\(2000\)112<278:MCOTSL>2.0.CO;2](https://doi.org/10.1130/0016-7606(2000)112<278:MCOTSL>2.0.CO;2).
- Reiter, D., M. Leidig, S.-H. Yoo, and K. Mayeda, 2012, Source characteristics of seismicity associated with underground wastewater disposal: A case study from the 2008 Dallas-Fort Worth earthquake sequence: *The Leading Edge*, **31**, 1454–1460, doi: [10.1190/tle31121454.1](https://doi.org/10.1190/tle31121454.1).
- Roback, R. C., 1996, Characterization and tectonic evolution of a Mesoproterozoic island arc in the southern Grenville Orogen, Llano Uplift, Central Texas: *Tectonophysics*, **265**, 29–52, doi: [10.1016/S0040-1951\(96\)00145-X](https://doi.org/10.1016/S0040-1951(96)00145-X).
- Savvaidis, A., B. Young, G.-C. D. Huang, and A. Lomax, 2019, TexNet: A statewide seismological network in Texas: *Seismological Research Letters*, **90**, 1702–1715, doi: [10.1785/0220180350](https://doi.org/10.1785/0220180350).
- Scales, M. M., H. R. DeShon, M. B. Magnani, J. I. Walter, L. Quinones, T. L. Pratt, and M. J. Hornbach, 2017, A decade of induced slip on the causative fault of the 2015 M_w 4.0 Venus earthquake, northeast Johnson County, Texas: *Journal of Geophysical Research: Solid Earth*, **122**, 7879–7894, doi: [10.1002/2017JB014460](https://doi.org/10.1002/2017JB014460).
- Schultz, R. A., R. Soliva, H. Fossen, C. H. Okubo, and D. M. Reeves, 2008, Dependence of displacement-length scaling relations for fractures and deformation bands on the volumetric changes across them: *Journal of Structural Geology*, **30**, 1405–1411, doi: [10.1016/j.jsg.2008.08.001](https://doi.org/10.1016/j.jsg.2008.08.001).
- Schwab, D. R., T. S. Bidgoli, and M. H. Taylor, 2017, Characterizing the potential for injection-induced fault reactivation through subsurface structural mapping and stress field analysis, Wellington Field, Sumner County, Kansas: *Journal of Geophysical Research: Solid Earth*, **122**, 10–132, 154, doi: [10.1002/2017JB014071](https://doi.org/10.1002/2017JB014071).
- Seeber, L., J. G. Armbruster, and W. Y. Kim, 2004, A fluid-injection-triggered earthquake sequence in Ashtabula, Ohio: Implications for seismogenesis in stable continental regions: *Bulletin of the Seismological Society of America*, **94**, 76–87, doi: [10.1785/0120020091](https://doi.org/10.1785/0120020091).
- Shah, A. K., and G. R. Keller, 2017, Geologic influence on induced seismicity: Constraints from potential field data in Oklahoma: *Geophysical Research Letters*, **44**, 152–161, doi: [10.1002/2016GL071808](https://doi.org/10.1002/2016GL071808).
- Smye, K. M., C. R. Lemons, R. Eastwood, G. McDaid, and P. H. Hennings, 2019, Stratigraphic architecture and petrophysical characterization of formations for deep disposal in the Fort Worth Basin, TX: *Interpretation*, **7**, no. 4, SL1–SL17, doi: [10.1190/INT-2018-0195.1](https://doi.org/10.1190/INT-2018-0195.1).
- Sullivan, E. C., K. J. Marfurt, A. Lacazette, and M. Ammerman, 2006, Application of new seismic attributes to collapse chimneys in the Fort Worth Basin: *Geophysics*, **71**, no. 4, B111–B119, doi: [10.1190/1.2216189](https://doi.org/10.1190/1.2216189).
- TexNet Earthquake Catalog, <https://www.beg.utexas.edu/texnetcisr/texnet/earthquake-catalog>, accessed December 2019.
- Thomas, W. A., 2004, Genetic relationship of rift-stage crustal structure, terrane accretion, and foreland tectonics along the southern Appalachian-Ouachita Orogen:

- Journal of Geodynamics, **37**, 549–563, doi: [10.1016/j.jog.2004.02.020](https://doi.org/10.1016/j.jog.2004.02.020).
- Thompson, D. M., 1982, Atoka Group (Lower to Middle Pennsylvanian), northern Fort Worth Basin, Texas: Terrigenous depositional systems, diagenesis, and reservoir distribution and quality: The University of Texas at Austin, Bureau of Economic Geology, Report of Investigations No. 125.
- United States Geological Survey (USGS), 2018, Earthquake catalog, <https://earthquake.usgs.gov/earthquakes/search/>, accessed December 2019.
- Viele, G. W., and W. A. Thomas, 1989, Tectonic synthesis of the Ouachita orogenic belt, in R. D. Hatcher, W. A. Thomas, and G. W. Viele, eds., The Appalachian-Ouachita Orogen in the United States, Geology of North America, F-2: Geological Society of America, Boulder, Colorado, 695–728, <http://rock.geosociety.org/Store/detail.aspx?id=DNAGGNAF2>, accessed February 2020.
- Walker, N., 1992, Middle Proterozoic geologic evolution of Llano Uplift, Texas: Evidence from U-Pb zircon geochronometry: Geological Society of America Bulletin, **104**, 494–504, doi: [10.1130/0016-7606\(1992\)104<0494:MPGEOL>2.3.CO;2](https://doi.org/10.1130/0016-7606(1992)104<0494:MPGEOL>2.3.CO;2).
- Walper, J. L., 1982, Plate tectonic evolution of the Fort Worth Basin, in C. A. Martin, ed., Petroleum geology of the Fort Worth Basin and Bend Arch area: Dallas Geological Society, 237–253.
- Walsh, F. R., and M. D. Zoback, 2015, Oklahoma's recent earthquakes and saltwater disposal: Science Advances, **1**, e1500195, doi: [10.1126/sciadv.1500195](https://doi.org/10.1126/sciadv.1500195).
- Walsh, F. R., and M. D. Zoback, 2016, Probabilistic assessment of potential fault slip related to injection induced earthquakes: Application to north-central Oklahoma, USA: Geology, **44**, 991–994, doi: [10.1130/G38275.1](https://doi.org/10.1130/G38275.1).
- Walsh, F. R. I., M. D. Zoback, D. Pais, M. Weingarten, and T. Tyrell, 2017, FSP 1.0: A Program for Probabilistic Estimation of Fault Slip Potential Resulting from Fluid Injection, <https://scits.stanford.edu/software>, accessed February 2020.
- Weingarten, M., S. Ge, J. W. Godt, B. A. Bekins, and J. L. Rubinstein, 2015, High-rate injection is associated with the increase in U.S. mid-continent seismicity: Science, **348**, 1336–1340, doi: [10.1126/science.aab1345](https://doi.org/10.1126/science.aab1345).
- Whitmeyer, S. J., and K. E. Karlstrom, 2007, Tectonic model for the Proterozoic growth of North America Steven: Geosphere, **3**, 220–259, doi: [10.1130/GES00055.1](https://doi.org/10.1130/GES00055.1).
- Wilkerson, A., W. D. Carlson, and D. Smith, 1988, High-pressure metamorphism during the Llano orogeny inferred from Proterozoic eclogite remnants: Geology, **16**, 391–394, doi: [10.1130/0091-7613\(1988\)016<0391:HPMDTL>2.3.CO;2](https://doi.org/10.1130/0091-7613(1988)016<0391:HPMDTL>2.3.CO;2).
- Zhang, Y., M. Person, J. Rupp, K. Ellett, M. A. Celia, C. W. Gable, B. Bowen, J. Evans, K. Bandilla, P. Mozley, T. Dewers, and T. Elliot, 2013, Hydrogeologic controls on induced seismicity in crystalline basement rocks due to fluid injection into basal reservoirs: Groundwater, **51**, 525–538, doi: [10.1111/gwat.12071](https://doi.org/10.1111/gwat.12071).
- Zoback, M., 2012, Managing the seismic risk posed by wastewater disposal: Earth, **57**, 38–43.
- Zoback, M. L., and M. D. Zoback, 1989, Tectonic stress field of the continental United States, in L. C. Pakiser and W. D. Mooney, eds., Geological Society of America Memoir 172, 523–540.

Elizabeth A. Horne received a B.S. from Utah State University and a M.S. from Colorado School of Mines. She is a research scientist associate at the Bureau of Economic Geology, the University of Texas at Austin, where she is the structural interpretation specialist for the Center for Integrated Seismicity Research (CISR) consortium. Her research interests include integrating field and subsurface data sets to generate 3D water-tight structural framework models that can be used to determine the kinematic evolution of complex structural systems.

Peter Hennings is a research scientist at the Bureau of Economic Geology, the University of Texas at Austin, where he is the principal investigator at CISR and a lecturer in the Department of Geological Sciences. He worked in the petroleum industry for 25 years as a research scientist (Mobil Oil and Phillips Petroleum) and as a technical manager (ConocoPhillips).

Johnathon L. Osmond is a Ph.D. candidate in the Department of Geosciences, University of Oslo, Norway. Formerly at the University of Texas at Austin, he specializes in fault and trap analysis and structural modeling and is currently pursuing a Ph.D. focusing on structural derisking of CO₂ storage sites with the Norwegian CCS Research Centre at the University of Oslo, Norway.

Heather R. DeShon is a seismologist, an associate professor of geophysics, and the director of undergraduate studies at Southern Methodist University. Her research interests include earthquake location, seismic tomography, earthquake source physics, intraplate and induced earthquakes, subduction zone processes, and network and real-time operations.